Neocortical layer 4 in adult mouse differs in major cell types and circuit organization between primary sensory areas

Scala F.*[1,2], Kobak D.*[3], Shan S.[1,2], Bernaerts Y.[3], Laturnus S.[3], Cadwell C.R.[4], Hartmanis L.[5], Castro J. [1,2], Tan Z.H. [1,2], Sandberg R.[5], Berens P.[3,6], Jiang X.[1,2,7], Tolias A.S.[1,2,8]

[1] Department of Neuroscience, Baylor College of Medicine, Houston, TX, USA

[2] Center for Neuroscience and Artificial Intelligence, Baylor College of Medicine, Houston, Texas, USA

[3] Institute for Ophthalmic Research, University of Tübingen, Tübingen, Germany

[4] Department of Anatomic Pathology, University of California San Francisco, San Francisco, CA, USA

[5] Department of Cell and Molecular Biology, Karolinska Institutet, Stockholm, Sweden

[6] Department of Computer Science, University of Tübingen, Tübingen, Germany

[7] Jan and Dan Duncan Neurological Research Institute at Texas Children's Hospital, Houston,

[8] Department of Electrical and Computational Engineering, Rice University, Houston, Texas, USA

* Equally contributed

Corresponding authors: Andreas S Tolias astolias@bcm.edu

Abstract

Layer 4 (L4) of mammalian neocortex plays a crucial role in cortical information processing, yet a complete census of its cell types and connectivity remains elusive. Using whole-cell recordings with morphological recovery, we identified one major excitatory and seven inhibitory types of neurons in L4 of adult mouse visual cortex (V1). Nearly all excitatory neurons were pyramidal and almost all Somatostatin-positive (SOM^+) neurons were Martinotti cells. In contrast, in somatosensory cortex (S1), excitatory cells were mostly stellate and SOM^+ cells were non-Martinotti. These morphologically distinct SOM^+ interneurons correspond to different transcriptomic cell types and are differentially integrated into the local circuit with only S1 cells receiving local excitatory input. Our results challenge the classical view of a canonical microcircuit repeated through the neocortex. Instead we propose that cell-type specific circuit motifs, such as the Martinotti/pyramidal pair, are optionally used across the cortex as building blocks to assemble cortical circuits.

Main

The mammalian sensory neocortex is organized in a six-layered structure. In this stereotypical architecture, layer 4 (L4) is the main target of sensory inputs coming from the thalamus, thus acting as the first level of cortical processing for sensory signals. Understanding how L4 implements its computations requires to characterize the diversity of its constituent neuronal components and the connectivity among them.

Most previous studies of L4 have focused on primary somatosensory cortex (S1) of young rats and mice. Spiny stellate cells have been reported to be the dominant excitatory neural type, both in rat [1,2] and in mouse after postnatal day five (as a result of sculpting of initially pyramidal neurons during development) [3]. In contrast, inhibitory interneurons are highly diverse in terms of their genetic markers, morphologies and electrophysiological properties. Previous studies have reported three types of fast-spiking (FS), parvalbumin-positive (PV^+) interneurons [4] and five types of non-FS interneurons [5], all of which have distinct morphologies. Several recent studies revealed that the somatostatin-positive (SOM^+) interneurons form a single morphological population that has been called non-Martinotti cells [6] since their axons mainly target L4 [7,8], in contrast to typical Martinotti cells, which target L1. Interneuron types exhibit type-specific connectivity patterns. For example, PV^+ FS interneurons receive thalamic inputs [9–13] but SOM^+ non-FS interneurons do not [14]. Both groups are reciprocally connected to local excitatory neurons and between each other [4,8,10,12,15,16], but PV^+ inhibit each other while SOM^+ do not [17].

Since most of these detailed studies were performed in S1 of young animals, it is unclear whether the cellular components of L4 and their connectivity profile are the same in other cortical areas and in adult animals. Recent large-scale studies of transcriptomic cell types in mouse and human cortex showed that most interneuron types are shared between cortical areas while the excitatory types are predominantly area-specific [18,19]. In line with this, a recent

study suggested a possible lack of spiny stellate cells in L4 of mouse primary visual cortex (V1) [20], in contrast to S1 L4. However, there has been no systematic comparisons of morphologies, electrophysiological properties and connectivity profiles between L4 of different cortical areas, leaving an open question about the similarity in their cellular components and circuitry.

To address this question, we used mouse V1 L4 as a model to compare with S1 L4. We performed a thorough census of the morphologically defined cell types in V1 L4 of adult mice (older than postnatal day 60, >p60) using multicellular simultaneous whole-cell recordings combined with post-hoc morphological recovery [21]. We identified several key differences in the cellular composition of L4 in V1 compared to S1, which we verified using targeted recordings of certain cell types in adult mouse S1 L4. In addition, we mapped some of the observed morphological cell types to a reference transcriptomic cell type atlas [18] using Patch-seq [22-24]. We further investigated the local connectivity profiles in both V1 and S1, finding similarities as well as some important differences in their circuitry.

Results

Morphologically defined cell types in L4 of adult mouse visual cortex

We characterized the electrophysiological and morphological features of L4 neurons in V1 of adult mice (≥2 months old, *n*=129) using whole-cell patch-clamp recordings combined with post-hoc morphological recovery (see Methods). Altogether, we recovered and analyzed the morphology of *n*=1174 neurons (578 excitatory, 596 inhibitory).

Out of the 578 excitatory cells, 573 (99.1%) were pyramidal neurons (PYR), characterized by apical dendrites extending into layer 1 (L1), consistent with one previous study [20]. These neurons did not show a complex arborization in L1, differing from typical layer 5 (L5) pyramidal neurons which generally have a prominent tuft [25–27] (Fig. 1A). Only five (0.9%) of the excitatory neurons were classified as spiny stellate cells based on the absence of the apical dendrites extending out of L4 to supragranular layers. These stellate cells had symmetrical non-polarized dendritic structure [1] (Fig. 2A). The prevalence of PYRs among excitatory neurons in L4 of V1 was further supported by the fact that all labeled neurons recorded in Scnn1a-Cre/Ai9 mice (*n*=5), in which excitatory neurons in L4 are selectively labeled [28,29], were morphologically confirmed as PYRs (100%, 30/30). In terms of electrophysiology, PYRs exhibited large action potential (AP) width, high AP amplitude, and shallow afterhyperpolarization (AHP) which clearly discriminate them from GABAergic interneurons (Fig. 2, S1, S2).

Interneurons showed a greater variability in both morphological and electrophysiological features. We used Viaat-Cre/Ai9 mice (*n*=47) to target GABAergic interneurons [30,21]. Almost all labeled neurons recorded from these mice (95.5%, 234/245) were morphologically confirmed as interneurons, with only a small fraction (4.5%) of PYRs. On the other hand, all unlabeled neurons (*n*=133) were morphologically confirmed as excitatory neurons, suggesting that the

entire population of interneurons in L4 was labeled in this Cre line. We identified seven different GABAergic cells types (Fig. 1) based on their morphology, following a widely used classification scheme based on the axonal geometry and projection patterns [21,31-33]: basket cells (BCs), Martinotti cells (MCs), bipolar cells (BPCs), neurogliaform cells (NFCs), shrub cells (SCs), double-bouquet cells (DBCs), and horizontally elongated cells (HECs). These morphological types varied greatly in abundance (Fig. 1) and electrophysiological properties (Fig. 2, S2).

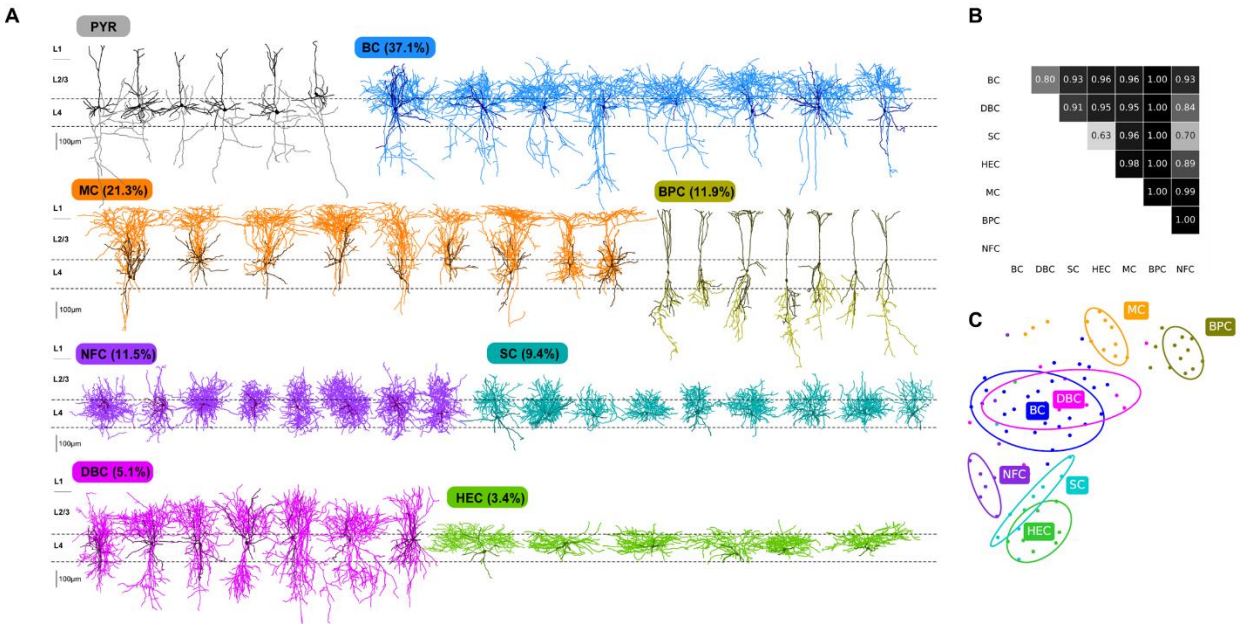

Figure 1: Morphologically defined neural types in V1 L4. (A) Representative morphologies for each cell type. The dendrites are shown in a darker shade of color and the axons in a lighter shade. For each interneuron type, its proportion among the morphologically identified interneurons in Viaat-Cre/Ai9 mice is indicated. **(B)** Cross-validated pairwise classification accuracy (using regularized logistic regression on a diverse set of morphological features) for each pair of cell types. Total sample size *n*=92. **(C)** 2D visualisation of the same *n*=92 cells in the space of morphological features using t-SNE. Ellipses show 80% coverage assuming 2D Gaussian distributions and using robust estimates of the mean and the covariance (i.e. ellipses do not include outliers).

BCs were the most abundant interneuron type (34.6%, 88/234). Somata of these neurons were usually larger than those of other L4 neurons. Their dendrites projected vertically in a bi-tufted manner, without a complex horizontal structure. The most salient morphological feature of BCs was a thick axon originating from the apical side of the soma. It typically projected towards L2/3 before forming a series of major branches that extensively spread above the apical region of the soma with few branches projecting horizontally and vertically downward to L5. All BCs exhibited a fast-spiking (FS) firing pattern with narrow AP width and high maximal firing rate (Figs. 2, S2).

MCs (20%, 47/234) were similar to those previously described both in developing cortex and in mature cortex in other layers [21,34-36]. They had bi-tufted dendrites with vertically or obliquely oriented branches. All of them had an ascending axon that projected to L2/3 and L1, where it ramified horizontally and formed a dense axonal cluster of variable extension. A small subset of MCs (8.9%, 11 out of all 124 recovered MCs) showed a secondary axonal cluster that extensively ramified around the soma within L4 (e.g. the last two MCs in Fig. 1). Firing pattern and electrophysiological properties showed a strong correspondence to L2/3 and L5 MCs described in both adult [21] and developing cortex [34]. In particular, these neurons were distinguished from other interneurons by their large membrane time constant (Fig. 2, S2).

BPCs (12.4%, 29/234) had a small soma and bipolar dendrites projecting to L1 and L5. The ascending dendrites formed a tuft in L1, similar to the structure of apical dendrites of PYRs. However, their dendrites lacked dendritic spines. The axon emerged from one of the descending dendrites and projected predominantly to L5. All BPCs showed an irregular-firing pattern associated with a high input resistance and large AP amplitude (Fig. 2, S2).

143 NFCs (12.7%, 27/234) were characterized by a very thin axon that highly ramified and formed a
144 dense arborization around cell bodies. These neurons fired late-spiking action potentials with
145 large AP width and high AP threshold (Fig. 2, S2).
146
147 SCs (9.4%, 22/234) were similar to the shrub cells that have been previously found in L5 of
148 adult mouse [21] and small BCs in L2/3 and L4 of young rats [37]. These neurons had non-polarized
149 dendritic branches mostly residing in L4 and thick axons often emerging from the apical region
150 of the cell bodies and branching locally around their soma. All SCs exhibited an FS firing pattern
151 (Fig. 2, S2).
152
153 DBCs (5.7%, 13/234) had large cell bodies and vertically-oriented bi-tufted dendrites, similar to
154 BCs. However, unlike BCs, the thick axon emerged often from the bottom of the soma,
155 projecting shortly towards L5 and forming several branches that projected upwards to L2/3 and
156 downwards to L5 with variable distances. Notably, the axons of these cells extended also
157 horizontally into L2/3 and L5, differing slightly from DBCs previously described in L2/3 [21]. All
158 DBCs exhibited an FS firing pattern (Fig. 2, S2).
159
160 HECs (3.5%, 8/234), with their horizontally extended axonal branches, were similar to the HECs
161 previously reported in L5 [21,38]. In particular, the axon had a thick primary structure that often
162 emerged from the apical side of the soma and bifurcated into secondary structures that spread
163 horizontally mostly within L4. All HECs exhibited an FS firing pattern (Fig. 2, S2).
164
165 We also performed experiments using several additional Cre-lines (parvalbumin-expressing,
166 PV-Cre/Ai9, *n*=31; somatostatin-expressing, SOM-Cre/Ai9, *n*=14; and expressing vasointestinal
167 peptide, VIP-Cre/Ai9, *n*=8) to relate genetic markers with morphological cell types (Fig. S3). The
168 majority of morphologically recovered PV^+ neurons were BCs (77.3%, 126/163 in PV-Cre/Ai9)

and the rest were SCs (9.2%, 15/163), DBCs (12.3%, 20/163), and HECs (1.2%, 2/163). The majority of SOM^+ neurons were typical MCs (91.8%, 56/61 in SOM-Cre/Ai9), while a small fraction exhibited an FS firing pattern and their morphological features matched those of BCs (8.2%, 5/61). All VIP^+ neurons in V1 L4 were BPCs (100%, 26/26 in VIP-Cre/Ai9).

To support our expert classification, we fully reconstructed a subset of neurons from each inhibitory type (*n*=92 in total) and trained a regularized logistic regression classifier to discriminate between each pair of inhibitory cell types (Fig. 1B, see Methods). We used a set of diverse morphological features (see Methods and Fig. S4) that we recently benchmarked elsewhere (Laturnus et al.; manuscript in preparation). Across all 21 pairs, the average cross-validated accuracy was 0.92, with most pairs discriminated almost perfectly. However, SC/HEC and SC/NFC pairs showed only ~0.65 classification accuracy. Visualisation of this dataset with t-SNE (Fig. 1C) indicated that SC/HEC and SC/NFC types were partially overlapping, as well as BC/DBC. Overall, this analysis suggests that while most morphological classes can be very well discriminated, some may be partially overlapping with intermediate cells showing ambiguous morphology. An important caveat is that low classification accuracy can also be due to an insufficient sample size.

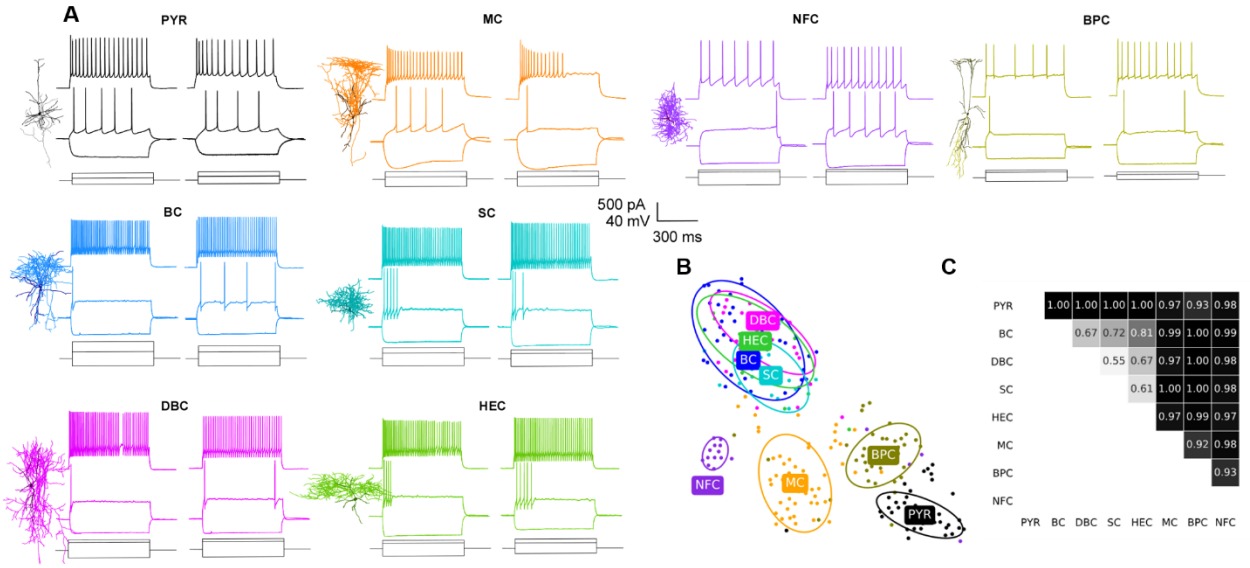

Figure 2: Electrophysiology of morphologically defined neural types in V1 L4. (A) Two exemplary electrophysiological traces for each of the eight morphologically defined cell types. The traces were used to automatically extract twelve electrophysiological features used for analysis shown in (B) and (C). **(B)** 2D visualisation of *n*=235 cells in the space of electrophysiological features using t-SNE. Ellipses show 80% coverage assuming 2D Gaussian distributions and using robust estimates of the mean and the covariance (i.e. ellipses do not include outliers). **(C)** Cross-validated pairwise classification accuracy (using regularized logistic regression) for each pair of cell types. Total sample size *n*=235.

To further explore variability in firing properties between cell types, we characterized the firing pattern of a subset of neurons (*n*=235) using twelve automatically extracted electrophysiological features (Fig. S1). Most features exhibited strong differences between cell types (Fig. S2). Two-dimensional visualisation of this dataset using t-SNE (Fig. 2B) showed that all four PV^+ cell types overlapped in one group of electrophysiologically similar FS neurons, while the other four types (PYR, NFC, BPC, and MC) each had distinct firing patterns. We confirmed this using pairwise classification with regularized logistic regression (Fig. 2C): the average cross-validated

204 classification accuracy between the FS types was 0.67, while the average accuracy across all
205 other pairs was 0.98.
206
207 **V1 differs from S1 in major L4 cell types**
208 Although spiny stellate cells have been reported to be the predominant excitatory neurons in L4
209 of monkey, cat, and ferret V1 [3,39-42] we found that 98% of excitatory cells in L4 of mouse V1
210 were PYRs (see above; Fig. 3A), confirming one previous report [20]. This is different from S1
211 where stellate cells were found to be abundant in L4 of young rats [1,43] and mice [3]. To confirm
212 that stellate cells were also abundant in S1 V4 of adult mouse, we additionally recovered L4
213 excitatory cells in S1 (*n*=24 mice) with the same method as in V1. We found that indeed 76.6%
214 (85/114) of the recovered spiny neurons did not have a clear apical dendrite and were thus
215 classified as stellate cells (Fig. 3B). In particular, in Scnn1a-Cre/Ai9 mice (*n*=5), we detected
216 only four PYRs among twenty six labeled and morphologically recovered excitatory cells (PYR:
217 15.3%, 4/26; Stellate: 84.7%, 22/26). This confirms that, unlike in V1, stellate cells are the
218 predominant excitatory population in L4 of adult S1 (Fisher's exact test for difference in the
219 fraction of stellate cells between V1 and S1: $p<0.0001$; 85/114 vs. 11/585).
220
221 Recent evidence indicates that most, if not all, L4 SOM^+ cells in mouse S1 have axons
222 restricted within L4, in stark contrast to typical MCs [8]. Indeed, we found that in S1, almost all L4
223 SOM^+ neurons we recovered had non-MC morphology characterized by a thin, highly ramifying
224 axon [44] mostly residing within L4 (Fig. 3B). Only two cells showed an ascending axon projecting
225 to L1 typical of MCs (2/79) and one was characterized by a thick axon branching similarly to BC
226 with a FS firing pattern (1/79) (Fisher's exact test for difference in the fraction of NMCs between
227 S1 and V1: $p<0.0001$; 76/79 vs. 0/61). We follow the convention of a previous study [6] and refer
228 to these SOM^+ neurons that dominate L4 in S1 as non-Martinotti cells (NMCs). These neurons

also differed in their firing pattern from MCs recorded in V1: e.g. they had a higher maximal firing rate (Fig. 4A; see also below).

To further investigate the differences between MCs in V1 and NMCs in S1, we used the Patch-seq [22-24] technique combining patch-clamp recordings with single cell transcriptomics. We sequenced RNA of SOM$^+$ neurons in L4 of V1 and S1 (n=71 after quality control, n=36 in V1 and n=35 in S1). We obtained on average 1.1 million reads per cell (median; mean±SD on a log10 scale: 6.1±0.2) and detected 6.3±1.6 thousand (mean±SD) genes per cell (Fig. S5). We mapped these cells to a large transcriptomic cell type dataset [18] that contained 21 somatostatin clusters with 2880 neurons from V1 and ALM. The quality of the mapping was equally good for V1 and S1 cells (Fig. S5), suggesting that the V1+ALM dataset is a reasonable reference for S1 interneurons. This is in agreement with the idea that inhibitory transcriptomic cell types are shared across cortical regions [18,19].

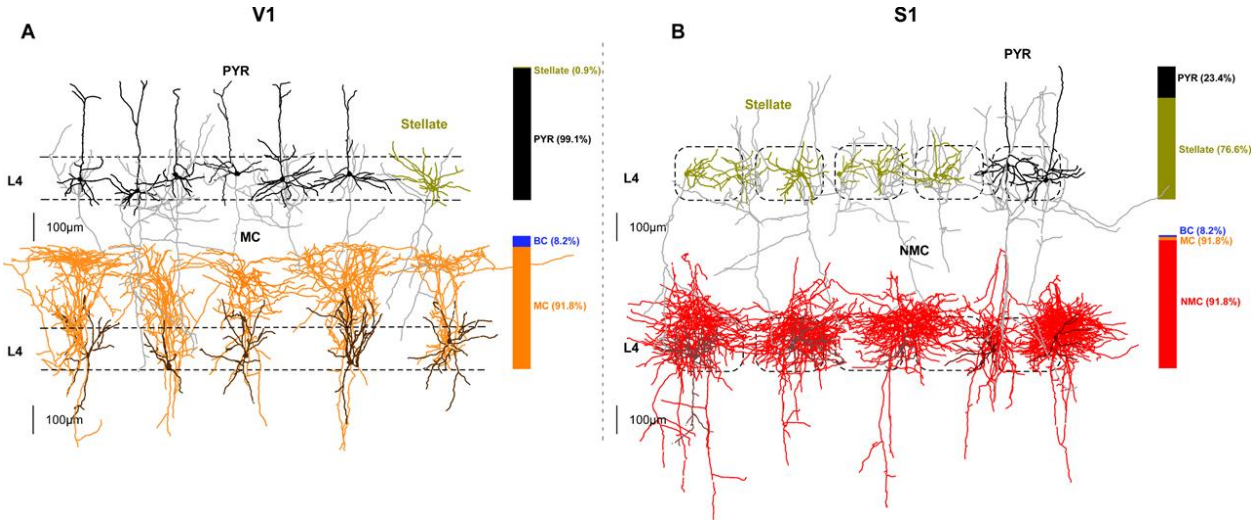

Figure 3: V1 differs from S1 in excitatory cells and SOM$^+$ interneurons in L4. (A) Representative morphologies of excitatory and SOM$^+$ neurons in V1 L4. Bar graphs indicate the fractions of each cell type among all morphologically recovered excitatory neurons (top) and all morphologically recovered SOM$^+$ neurons (bottom). **(B)** The same in S1 L4. Dashed rectangles represent individual cortical barrels.

Most cells (80%, 57/71) were assigned to one of the two clusters: *Sst Calb2 Pdlim* and *Sst Hpse Cbln4* (Fig. 4B-C), with S1 cells falling almost exclusively into the *Hpse* cluster (27/29) and V1 cells falling preferentially into the *Calb2* cluster (20/28) ($p<0.0001$ with Fisher's exact test). This suggests that *Sst Calb2 Pdlim* is a MC cluster, in agreement with the conclusions of Tasic et al. [18] based on the data from Paul et al. [45], and that *Sst Hpse Cbln4* is a NMC cluster, in agreement with Naka et al. [46] However, this raises the question of why some V1 L4 SOM$^+$ cells, which all have MC morphology (see above), had a NMC transcriptomic profile, both among our Patch-seq cells and in the Tasic et al. dataset.

To answer this question, we looked at electrophysiological features that were most different between SOM$^+$ interneurons in V1 and S1 (Cohen's $d>1$: input resistance, membrane time constant, maximum firing rate, and AP width) and found that for two of them (input resistance and membrane time constant) V1 cells belonging to the *Hpse* cluster had values more similar to the S1 cells than to the V1 cells from the *Calb2* cluster (Fig. 4D). This suggests that electrophysiologically, V1 *Hpse* MC cells are in between V1 *Calb2* MC cells and S1 NMC cells.

The relationship between gene expression and electrophysiological features can be visualized using the sparse reduced-rank regression analysis that we have recently introduced [47]. This technique aims to reconstruct all the electrophysiological features using a two-dimensional projection of the expression levels of a small set of genes (Fig. 4E). This analysis supports our conclusion that V1 *Hpse* MCs are "in between" MCs and NMCs in terms of electrophysiology. Interestingly, this analysis also shows that cells falling in the *Tac1* and *Mme* clusters tend to have a distinct firing pattern which is different from firing patterns of MCs and NMCs. These

three transcriptomic cell types have recently been identified in Tasic et al. [18], and do not have known morphological or electrophysiological counterparts.

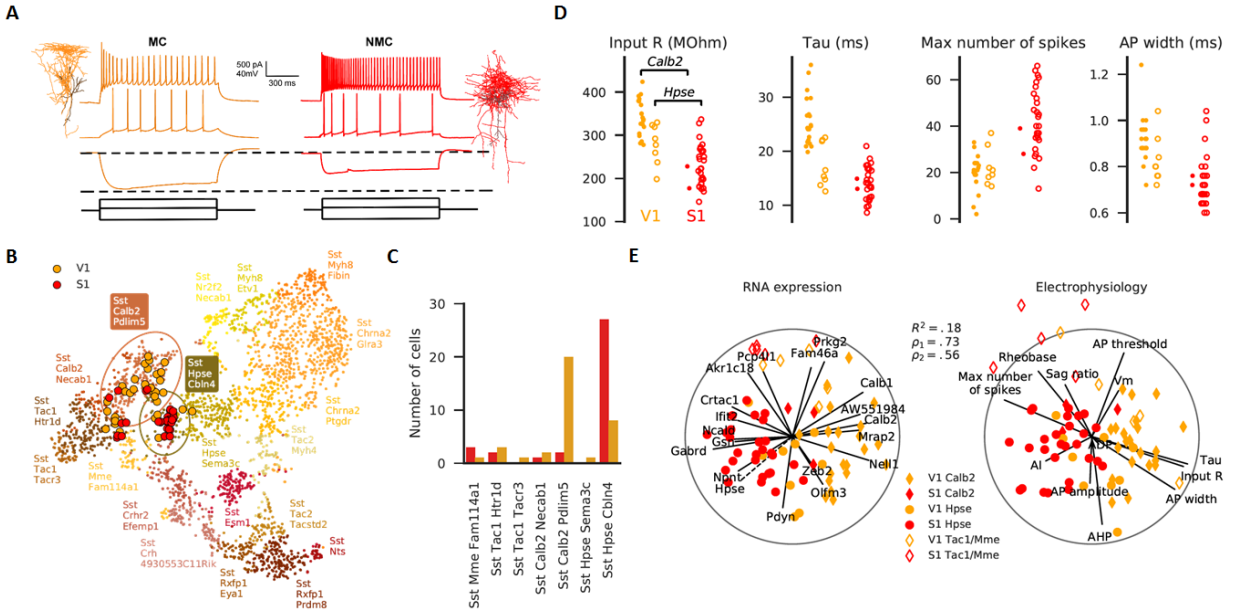

Figure 4: SOM$^+$ interneurons in L4 of V1 and S1 differ in electrophysiological properties and transcriptomic profile, as shown by Patch-seq. (A) Morphologies and firing patterns of two exemplary cells, from V1 (orange) and S1 (red) respectively. **(B)** Mapping of the Patch-seq cells (*n*=71) to the t-SNE visualization of the transcriptomic diversity among *Sst* clusters from Tasic et al. [18] t-SNE was done on all cells from *Sst* clusters except for *Sst Chodl* that is very well separated from the rest (20 clusters; *n*=2701 cells), using 500 most variable genes (see Methods). Two ellipses show 90% coverage areas of the two clusters where the most Patch-seq cells land. Mapping to t-SNE was performed as we described elsewhere [48], see Methods. **(C)** Cluster assignment of the Patch-seq cells. There is a very good correspondence between (B) and (C). **(D)** Four electrophysiological features that differed most strongly (Cohen's *d*>1) between V1 and S1 cells. Only cells assigned to *Sst Calb2 Pdlim5* and *Sst Hpse Cbln4* clusters are shown. Note that the values are not directly comparable to those shown in Fig. S2 because Patch-seq experiments used a different internal solution compared to regular patch-clamp experiments without RNA extraction. **(E)** Sparse reduced-rank regression analysis [47]: the left biplot shows two-dimensional projection in the transcriptomic space that is optimized to reconstruct the electrophysiological

features. The right biplot shows the corresponding two-dimensional projection in the electrophysiological space; it should "match" to the left plot if the model is accurate. Color denotes brain area (orange for V1, red for S1), marker shape denotes transcriptomic cluster that each cell was assigned to (circles for the two *Hpse* clusters, diamonds for the two *Calb2* clusters, open diamonds for the three *Tac1/Mme* clusters). Individual features are depicted with lines showing their correlations to the two components. Circles show maximal possible correlation. R^2, ρ_1, and ρ_2 refer to cross-validated estimates of the overall R-squared and correlations between the horizontal and vertical components.

We additionally performed Patch-seq recordings of L5 SOM$^+$ cells in both areas and found that while they mapped to a different set of transcriptomic clusters than the L4 SOM$^+$cells (Fig. S5), there were no systematic differences between S1 and V1 in terms of transcriptomic cell types.

Connectivity among excitatory and SOM$^+$ neurons in L4 of V1 vs. S1

So far, we have described major differences in the morphology, electrophysiology, and transcriptomic signatures of excitatory neurons and SOM$^+$ interneurons in L4 between V1 and S1. We next investigated whether there are differences in their connectivity profiles as well, using simultaneous multi-cell patch-clamp recordings. We found that certain connectivity patterns between them are very similar across both areas (Fig. 5). First, the connection probabilities among excitatory cells were low in both areas (1.0%, 7/701 in V1; 2.5%, 3/122 in S1). Second, the connection probabilities between SOM$^+$ cells were also low in both areas (0%, 0/68 in V1; 3.8%, 2/52 in S1). Third, the connection probabilities from SOM$^+$ cells to excitatory cells were high in both areas (21.1%, 30/142 in V1, 26.6%, 17/64 in S1). In addition, despite their low connectivity via chemical synapses, both MCs in V1 and NMCs in S1 were similarly often interconnected by gap junctions (MCs: 23.5%, 8/34; NMCs: 30.7%, 8/26; Fig. S6).

On the other hand, we found a striking difference between the areas in connection probabilities from excitatory to SOM^+ neurons. In S1, NMCs received facilitating synaptic connections from local excitatory neurons (12.5%, 8/64), in line with previous studies in young rodents [8,10]. In contrast, we did not find any connections (0%, 0/142) from local excitatory neurons to MCs in V1 (p=0.0002, Fisher's exact text). This was in stark contrast to MCs in L2/3 and L5 of adult mouse V1, which receive strong input from local PYRs in the same layers [21] (see Discussion for further considerations).

In addition, we tested the connectivity pattern of BCs in V1 L4, in order to complete the connectivity matrix between the three most abundant types: PYRs, BCs, and MCs (Fig. S8). We found that BCs followed the same connectivity rules as previously found in other layers for basket cells [21,49]. PYRs connected to BCs with probability 12.5% (38/303), MCs inhibited BCs with probability 32.6% (15/46), and BCs inhibited each other (36.7%, 75/204), MCs (13.0%, 6/46) and PYRs (25.7%, 78/303). All of these connections have also been reported in S1 L4 of young mice [17]. We also found that BCs were electrically coupled to each other with probability 27.5% (28/102), in agreement with previous findings that gap junctions exist between inhibitory cells of the same type [50].

Notably, the connection probability between PYRs in V1 L4 was very low, consistent with our previous work in other layers in adult animals [21], but in contrast to the findings in young and juvenile rodents [51,52]. To confirm that this low connectivity reflects an age effect, we measured the connectivity between PYRs in V1 L4 at different ages (p15-p20 and p30-p40, n=5 each) using Scnn1a-Cre/Ai9 mice. We found that the connectivity probability monotonically decreased with age (Fig. S9): from 13.2% in p15-p20 (15/114) to 5.1% in p30-p40 (8/156) to 1.0% in >p60 reported above (7/701).

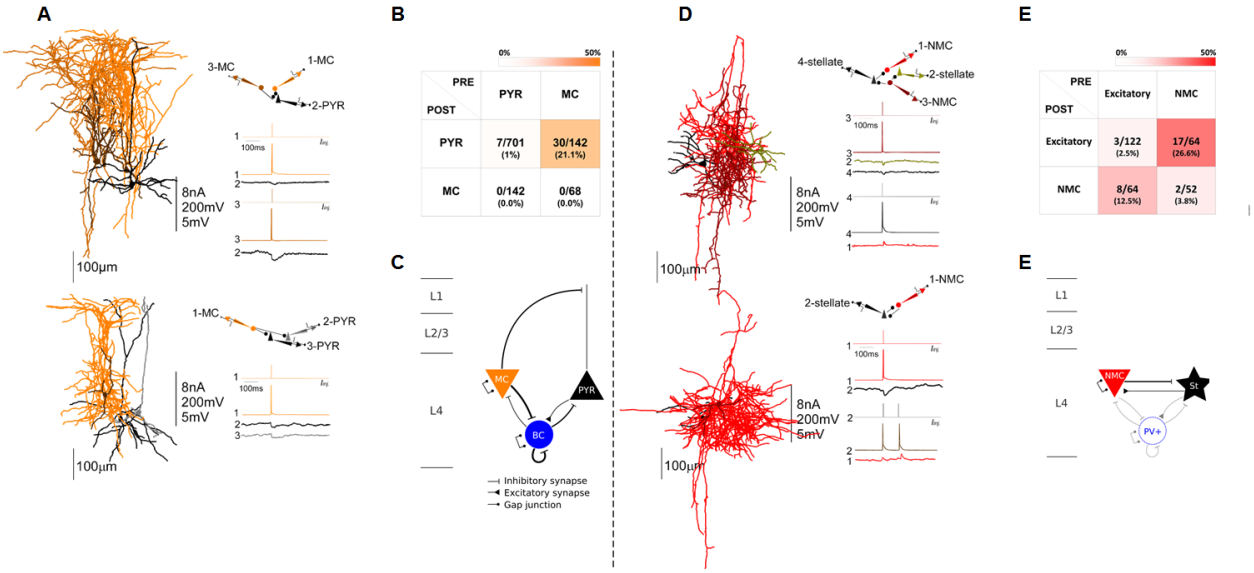

Figure 5: Connectivity between excitatory and SOM$^+$ cells in L4 of V1 and S1. (A) Examples of simultaneous recordings from excitatory and SOM$^+$ neurons in V1 L4. Recorded neurons were close to each other (generally less than 150µm). Vertical scale bar indicates: amplitudes of injected current in nA, amplitude of APs in mV and amplitude of uEPSP or uIPSP in mV. **(B)** Color coded connectivity matrix shows the connection probability between cell types as a percentage of tested potential connections. Average of uEPSP and uIPSP as well as PPR are reported in Fig. S7. **(C)** Schematic of the local circuitry in L4 V1. For the connectivity involving BCs, see Fig. S8. For gap junctions, see Fig. S4. Line thickness corresponds to connection probability. **(D-F)** The same for L4 S1. In the schematic in panel (F), connectivity involving BCs is taken from Ma et al. [17] All these BCs connections are shown with the same strength as that study used juvenile (p15) mice and so connection strengths are not directly comparable to the values obtained in our experiments. Regarding gap junctions between FS interneurons see also [50,53].

Discussion

Morphological cell types in L4: V1 vs. S1

We described eight morphological neuronal types in V1 L4 of adult mice as well as the connectivity patterns of three most abundant cell types. We found that nearly all excitatory neurons are pyramidal cells, in stark contrast to S1 L4 where the majority of excitatory neurons are stellate cells [1,3,43]. Interestingly, L4 stellate cells in ferret V1 and mouse S1 develop postnatally from neurons that resemble pyramidal cells with an upward projecting apical dendrite [3]. The near absence of stellate cells in V1 L4 of adult mice (as old as 12 months in our experiments) suggests a different developmental mechanism in this case. One previous study [20] also reported mostly pyramidal cells in mouse V1 L4, but considered this result indecisive due to a possible selection bias. Our results in S1 show that selection bias (if any) does not prevent us from finding stellate cells, and suggest that the observed prevalence of pyramidal cells in adult V1 L4 is real. It remains an open question, why pyramidal cells in mouse V1 L4 remain pyramidal, whereas L4 excitatory cells in mouse S1 and in V1 of other non-rodent species develop into stellate cells.

We also found that almost all SOM$^+$ neurons in V1 L4 are Martinotti cells, which is also in contrast to S1 L4, where almost all SOM$^+$ neurons are non-Martinotti [7,8]. Using Patch-seq, we showed that SOM$^+$ MCs in V1 L4 and SOM$^+$ NMCs in S1 L4 correspond to two different transcriptomic cell types (*Sst Calb2 Pdlim* and *Sst Hpse Cbln4* respectively) previously identified in a large-scale transcriptomic cell atlas [18].

We relied on manual expert classification to isolate the morphological types. Unlike in transcriptomics, where automatic unsupervised clustering is commonplace [18], morphological

studies usually do not use it, because of low numbers of manually reconstructed neurons and multiple challenges to data analysis of morphological data. One recent study done in parallel to our work [54] attempted clustering of neural morphologies from all layers of adult mouse V1. There is a broad agreement between their types from L4 and our types. There are also some differences: they split abundant types (e.g. PYRs and BPCs) into multiple narrow sub-clusters, while at the same time missing some rare types such as HECs.

Transcriptomic types of SOM$^+$ interneurons in L4: V1 vs. S1

Although MCs and NMCs are morphologically distinct, with no ambiguous morphological forms, they form more of a continuum in both transcriptomic and electrophysiological space. In the Tasic et al. reference dataset [18], the MC and the NMC clusters (*Sst Calb2 Pdlim* and *Sst Hpse Cbln4* respectively), although distinct, were close and partially overlapping in the t-SNE visualisation (Fig. 4B). Consistent with this, Tasic et al. [18] also found intermediate cells between the “core” members of these two clusters. We show that, electrophysiologically, MCs and NMCs also form a continuum (Fig. 4E) with all electrophysiological features having unimodal distributions (Fig. 4D). This is in agreement with the findings of Naka et al. [46] who demonstrated an electrophysiological continuum between NMCs in S1 L4 and MCs in S1 L5. How these cells develop sharply distinct morphologies given overlapping transcriptomic and electrophysiological profiles, is an interesting open question.

Even though we did not identify any NMCs in V1, the transcriptomic reference dataset [18] contained many V1 cells from the *Sst Hpse Cbln4* cluster, and we found that some MCs from V1 had transcriptomic profile mapping to this cluster. These cells show an electrophysiological profile intermediate between MCs and NMCs, but morphologically correspond to MCs based on our data. We hypothesize that these cells may be “latent NMCs”, present in V1, but failing to develop a NMC morphology due to the nearly complete absence of stellate cells in V1. Tasic et

al. [18] showed that the majority of transcriptomic inhibitory types are shared between two very different cortical areas (V1 and ALM). Our findings demonstrate that this does not necessarily imply that morphological types are also all shared.

Using Patch-seq, we also performed single-cell RNA-sequencing on a small number of L5 SOM^+ cells in both S1 and V1. Morphologically, all L5 SOM^+ cells in these two cortical areas are known to be MCs [21,46]. We found that they had electrophysiological features similar to L4 MCs (Fig. S5), but mostly mapped to a different set of transcriptomic clusters than the L4 SOM^+ cells (Fig. S5). These results identify five transcriptomic clusters from Tasic et al. [18] as L5 MCs, but the differences between these clusters remain unclear. We also found several SOM^+ cells, mostly in L4, that mapped to the *Sst Tac2* and *Sst Mme* transcriptomic clusters. Some of these cells had very distinct electrophysiological profile (Fig. 4E). Our results suggest that a fraction of MCs and NMCs in L4 can belong to these three transcriptomic types. The identity and the role of these cells remains to be explored in the future.

Circuit organization in L4: V1 vs. S1

In terms of connectivity, both MCs in V1 and NMCs in S1 avoid connecting to each other (apart from forming gap junctions), and project to excitatory population in L4. Moreover, the axonal morphologies of these two cell types seemed to match the respective dendritic morphologies of their excitatory neuronal targets. In V1, axons of L4 MCs projected to L1 where they are potentially able to synapse onto the apical dendrites of L4 PYRs, similar to the pattern described in other cortical layers [55,56]. In S1, by contrast, axons of L4 NMCs were more localized, matching the more compact dendritic structure of stellate cells. This observation is in line with previous findings that the excitatory identity controls the survival and wiring of local interneurons [57,58]. Therefore, we hypothesize that the difference in SOM^+ cells between these two cortical areas might be a result of the difference in the population of excitatory neurons.

On the other hand, while we found that SOM$^+$ cells receive inputs from local excitatory neurons in S1 L4, in agreement with previous studies [8,17], we did not detect connections from L4 PYRs to L4 MCs in V1. SOM$^+$ Martinotti cells in other layers are known to receive facilitating excitatory inputs from local principal neurons in both S1 [59,60] and V1 [21,61]. However, our results suggest that L4 MCs in V1 behave differently. Interestingly, previous studies have also shown that in V1, L4 MCs do not receive direct input from LGN [14], while in L2/3 MCs do not receive input from L4 excitatory neurons [61]. Together with our results, this suggests that MCs in V1 are not directly recruited in the feed-forward pathway. Further investigations are needed to test whether L4 MCs in V1 are driven by PYRs in other layers or by long-range inputs from other areas.

In addition to the connectivity among PYRs and MCs in V1 L4, we tested connectivity of BCs, another major cell type in L4 (Fig. S8). We found that BCs in L4 followed the same connectivity rules as described for basket cells in other layers [21] and in younger animals [49]: BCs inhibit other BCs, MCs, and pyramidal cells, are inhibited by MCs and excited by PYRs. All of these connections have also been reported in S1 L4 in young mice [17], suggesting that the circuitry involving PV$^+$ cells is roughly conserved between these areas.

Finally, we found very low connection probability between PYRs in V1 L4, which was consistent with the findings in V1 L2/3 and V1 L5 of adult mice [21], but much lower than what was reported in young animals [62,63]. We directly show that this difference in connection probability among excitatory neurons is due to the age of the animal (Fig. S9).

Summary

In conclusion, we revealed differences in the morphologies of excitatory cells and SOM$^+$ interneurons in L4 of V1 and S1 of adult mice. In each area, the morphology of SOM$^+$

464 interneurons matched that of the excitatory neurons, opening the question of whether one of
465 them adapts to another or whether both are caused by a common regulatory mechanism. We
466 found differences in the connections from the excitatory population to the SOM^+ interneurons,
467 suggesting a different functional role of SOM^+ interneurons across areas and arguing against a
468 canonical local circuitry. In addition, we found that there is no one-to-one match between the
469 morphological and the transcriptomic types of SOM^+ interneurons, highlighting the need of multi-
470 modal profiling of neural types in the neocortex. Our results support the view that canonical
471 circuit motifs, such as the Martinotti/pyramidal pair, are used as optional building blocks to
472 assemble the neocortex, as opposed to a single canonical microcircuit repeated through all
473 cortical areas.

Methods

Data and code availability

Patch-seq data will be made available at https://www.ncbi.nlm.nih.gov/geo/. Apart from the raw reads, it includes a table of read counts, a table of RPKM values, and a table of the extracted electrophysiological features.

The analysis code in Python will be available at http://github.com/berenslab/L4-analysis. This includes data analysis of electrophysiological recordings, data analysis of the morphological reconstructions, and data analysis of the transcriptomic data. This repository also includes a table of the extracted electrophysiological features for the morphological data set.

Animals

Experiments on adult male and female mice (>2 months old) were performed using wild-type (*n*=24), Viaat-Cre/Ai9 (*n*=47), Scnna1-Cre/Ai9 (n=5), SOM-Cre/Ai9 (*n*=14), VIP-Cre/Ai9 (*n*=8), and PV-Cre/Ai9 mice (*n*=31). Crossing Viaat-Cre mice, that encode a transporter required for loading GABA and glycine, with Ai9 reporter mice globally labels GABAergic interneurons with the fluorescence marker tdTomato [30]. SOM-Cre/Ai9 mice, VIP-Cre/Ai9 mice, and PV-Cre/Ai9 mice have SOM^+ interneurons, PV^+ interneurons and VIP^+ interneurons labeled with the fluorescent marker tdTomato respectively. Scnn1a-Cre/Ai9 mice have excitatory neurons in L4 selectively labeled with tdTomato. Additional younger Scnn1a-Cre/Ai9 mice (p15-p20, *n*=5; p30-p40, *n*=5) were used to study connectivity between excitatory neurons at the different ages. Animal preparation procedures for animals maintenance and surgeries were performed according to protocols approved by the Institutional Animal Care and Use Committee (IACUC) of Baylor College of Medicine.

Slice preparation

Slice preparation followed methods previously described in Jiang et al. (2015). Briefly, animals were deeply anesthetized using 3% isoflurane. After decapitation, the brain was removed and placed into cold (0−4 °C) oxygenated NMDG solution containing 93 mM NMDG, 93 mM HCl, 2.5 mM KCl, 1.2 mM NaH_2PO_4, 30 mM $NaHCO_3$, 20 mM HEPES, 25 mM glucose, 5 mM sodium ascorbate, 2 mM Thiourea, 3 mM sodium pyruvate, 10mM $MgSO_4$ and 0.5 mM $CaCl_2$, pH 7.35. 300 µm thick parasagittal slices were cut and special care was taken to select only slices that had a cutting plane parallel to the apical dendrites to ensure preservation of both axonal and dendritic arborizations structures. The slices were incubated at 37.0±0.5 °C in oxygenated NMDG solution for 10-15 minutes before being transferred to the artificial cerebrospinal fluid solution (ACSF) containing: 125 mM NaCl, 2.5 mM KCl, 1.25 mM NaH_2PO_4, 25 mM $NaHCO_3$, 1 mM $MgCl_2$, 25 mM glucose and 2 mM $CaCl_2$, pH 7.4) for about 1 h. During recordings, slices were continuously perfused with oxygenated physiological solution throughout the recording session.

Electrophysiological recordings

Recordings were performed using patch recording pipettes (5−8 MΩ) filled with intracellular solution containing 120 mM potassium gluconate, 10 mM HEPES, 4 mM KCl, 4 mM MgATP, 0.3 mM Na_3GTP, 10 mM sodium phosphocreatine and 0.5% biocytin (pH 7.25). We used two Quadro EPC 10 amplifiers that allowed us to perform simultaneous recordings up to 8 cells. The PatchMaster software and custom-written Matlab-based programs were used to operate the Quadro EPC 10 amplifiers and perform online and offline analysis of the data. In order to extract information about passive electrical properties and firing patterns, neurons were stimulated with 600 ms long current pulses starting from -100 / -200 pA with 20 pA step. The holding current was not always 0 pA. For patch-seq recordings, the holding current was always 0 pA and the initial current was always -200 pA.

525

526 To identify synaptic connections, current pulses were injected into the presynaptic neurons (2
527 nA for 2 ms at 0.01–0.1 Hz) to evoke AP while post-synaptic membrane potential of other
528 simultaneously recorded neurons were monitored to detect unitary inhibitory or excitatory
529 postsynaptic potentials (uI(E)PSPs). The uIPSPs were measured while the membrane
530 potentials of the putative postsynaptic cells were held at −60±3 mV, whereas uEPSPs were
531 measured while membrane potentials of the putative postsynaptic cells were held at −70±3 mV.
532 Paired-pulse ratio (PPR) was calculated as the ratio between the mean amplitude of the second
533 and the first uEPSC obtained by injecting the presynaptic neuron with two consecutive stimuli of
534 2nA with 100ms interval. We recorded 10-30 individual traces average of which was used to
535 calculate uI(E)PSPs amplitude.
536 Neurons were assigned to L4 based on the neocortical layer boundaries and the identification of
537 the small somata that characterize this granular layer, which were clearly visible in the
538 micrograph under the bright-field microscope. The layer identity of each neuron was also
539 confirmed post-hoc by the visualization of their position after the staining.
540

541 Because the synaptic connectivity significantly depends on the inter-soma distance (Jiang et al.,
542 2015), we took special care to record from groups of neurons with inter-soma distances
543 generally less than 200 µm. To make sure that the identified connections were monosynaptic,
544 we morphologically confirmed post-hoc the presynaptic neurons for all connections and made
545 sure that the morphology and electrophysiology of the presynaptic neuron for each connection
546 (i.e. pyramidal neurons vs. interneurons) matched the nature of connections (i.e. EPSP vs.
547 IPSP). Indeed, the recovered morphology (i.e. pyramidal neurons vs. interneurons) and EPSP
548 vs. IPSP always matched.
549

Importantly, as a consequence of slicing procedure, neuronal structures can be severed (a limitation of all slice electrophysiology experiments) due to the slicing procedure introducing a significant underestimation of the morphology of neurons and connectivity. However, this did not seem to strongly influence the study of local circuits in the past [21,64].

Staining and morphology recovery

After the end of the patch-clamp recording, the slices were fixed by immersion in freshly-prepared 2.5% glutaraldehyde 4% paraformaldehyde in 0.1 M phosphate-buffered saline at 4°C for at least 72h. The slices were subsequently processed with the avidin-biotin-peroxidase method in order to reveal the morphology of the neurons. To increase the success rate in recovering the morphology of mature GABAergic interneurons, especially detail of their fine axonal arbors, we used additional modifications described in [21,22]. The morphologically recovered cells were examined and reconstructed using a 100X oil-immersion objective lens and a camera lucida system.

Patch-seq procedure and sequencing

To obtain electrophysiology and transcriptome data from single neurons, we used our recently described Patch-seq protocol [22] with the following additional modifications. Recording pipettes of 5 MΩ resistance were filled with RNase-free intracellular solution containing: 101 mM potassium gluconate, 4 mM KCl, 10 mM HEPES, 0.2 mM EGTA, 4 mM MgATP, 0.3 mM Na_3GTP, 5 mM sodium phosphocreatine, and 1 U/µl recombinant RNase inhibitor (Takara Cat.no. 2313A), pH ~7.25. The cDNA was amplified using 18 amplification cycles and the size distribution and concentration of the libraries were analyzed with an Agilent Bioanalyzer 2100. cDNA samples containing less than 1.5 ng total cDNA, or with an average size less than 1,500 bp were not sequenced (*n*=8 cells).

To construct the final sequencing libraries, 0.2 ng of purified cDNA from each sample was tagmented using the Illumina Nextera XT Library Preparation using ⅕ of the volumes stated in the manufacturer's recommendation. The DNA was sequenced from single end (75 bp) with standard Illumina Nextera i5 and i7 index primers (8 bp each) using an Illumina NextSeq500 instrument. Investigators were blinded to cell type during library construction and sequencing.

Reads were aligned to the mouse genome (`mm10` assembly) using STAR (v2.4.2a) with default settings. We only used read counts (and not RPKM values, number of reads per kilobase of transcript per million total reads) for all data analysis presented here, but for completeness we mention that RPKM values were computed using `rpkmforgenes` [65] and NCBI RefSeq gene and transcript models (downloaded on the 24th of June 2014).

Data analysis of the morphological reconstructions

Reconstructed morphologies of *n*=92 cells were converted into SWC format and further analyzed using custom Python code (see the github repository linked above). Each cell was soma-centered and rotated such that the *z* coordinate (height) was oriented along the cortical depth and the *x* coordinate (width) was oriented along the first principal component of the *xy* point cloud, i.e. roughly corresponded to the cell's largest extent in the plane orthogonal to the cortical depth. For further analysis we computed and combined three different feature representations of each cell: the XZ density map, the 2D persistence image, and a set of morphometric statistics (see below).

<u>XZ density map</u>

We sampled equidistant points with 100 nm spacing along each neurite and normalized the resulting point cloud such that the smallest coordinate across all points of all cells was 0 and the largest was 1 [66]. The normalized point cloud was projected onto the *xz*-plane and binned into

100×100 bins spanning [-0.1, 1.1]. We smoothed the resulting density map by convolving it with a 11×11 bin Gaussian kernel with standard deviation σ=2. For the purposes of downstream analysis, we treated this as set of 10,000 features.

2D persistence image

The persistence image is a fairly new morphological representation based on ideas from topology [67] . We briefly outline it here. Starting from each tip, one records "birth time" of each branch as the radial distance of the tip from the soma. While moving away from the tips towards the soma, at each branch-point the "younger" branch, i.e. the one with a smaller birth time, is "killed" and its "death time" is recorded. This results in a 2D point cloud of (*birth time*, *death time*) for each branch with only the longest branch surviving until the soma and having a death time of 0. We performed kernel density estimation of this point cloud using a 2D Gaussian kernel (`gaussian_kde` from the `scipy.stats` package with default settings). To create an image similar to the density map, we evaluated the density estimate on a 100×100 equidistant grid spanning a [0:*max_birth*, 0:*max_death*] rectangle. Here *max_birth* and *max_death* refer to the maxima across all cells (789 µm and 757 µm in our data respectively). For the purposes of downstream analysis, we treated this as set of 10,000 features.

Morphometric statistics

For each cell we computed a set of 16 summary statistics: number of branch points, cell width, cell depth, cell height, number of tips, number of stems, total neurite length, maximal neurite length, maximum branch order, maximal segment length, average tortuosity, maximal tortuosity, average branch angle, maximal branch angle, average path angle, and maximal path angle.

Pairwise classification

We followed the pipeline that we recently benchmarked elsewhere (Laturnus et al. 2018; manuscript in preparation). As predictors for pairwise classification we used morphometric statistics, density map and persistence image. Due to the very high dimensionality of the density map and the persistence image, we reduced each of them to 10 principal components (for cross-validation, PCA was computed on each outer-loop training set separately, and the same transformation was applied to the corresponding outer-loop test set). This makes the final feature dimensionality equal to 36.

For classification, we used logistic regression regularized with elastic net. Regularization parameter alpha was fixed to 0.5, which is giving equal weights to the lasso and ridge penalties. We used nested cross-validation to choose the optimal value of the regularization parameter lambda and to obtain an unbiased estimate of the performance. The inner loop was performed using the `civisanalytics` Python wrapper around the `glmnet` library [68] that does K-fold cross-validation internally. We used 5 folds for the inner loop. We kept the default setting which uses the maximal value of lambda with cross-validated loss within one standard error of the lowest loss (`lambda_best`) to make the test-set predictions:

```
LogitNet(alpha=0.5, n_splits=5, random_state=42)
```

Note that the default behavior of `glmnet` is to standardize all predictors. The outer loop was 10 times repeated stratified 5-fold cross-validation, as implemented in `scikit-learn` by

```
RepeatedStratifiedKFold(n_splits=5, n_repeats=10, random_state=43)
```

Outer-loop performance was assessed via test-set accuracy.

t-SNE

For the t-SNE visualization, we reduced density maps, persistence images, and morphometric statistics of the *n*=92 cells to 10 principal components each. We scaled each set of 10 PCs by

the standard deviation of the respective PC1, to make three sets be roughly on the same scale. Then we stacked them together to obtain a 30-dimensional representation of each cell. Exact (non-approximate) t-SNE was run with perplexity 15, random initialisation with seed 42, and early exaggeration 4, using `scikit-learn` implementation:

```
TSNE(perplexity=15, method='exact',
     random_state=42, early_exaggeration=4)
```

Automatic extraction of electrophysiological features

Thirteen electrophysiological features were automatically extracted using Python scripts from the Allen Software Development Kit (https://github.com/AllenInstitute/AllenSDK) with additional modifications to account for our experimental paradigms (see the github repository linked above). An illustration of the feature extraction procedure for one exemplary neuron is shown in Fig. S1. Here we briefly specify how each feature was extracted.

The resting membrane potential and the input resistance were computed differently for the patch-clamp/morphology recordings and for the Patch-seq recordings, because of the differences in the stimulation protocol between these two sets of experiments. In the Patch-seq experiments, the current clamp value before each current stimulation was fixed at 0 pA for all cells. Consequently, we computed the resting membrane potential as the median membrane voltage before stimulation onset. Input resistance for each hyperpolarizing stimulation was calculated as the ratio of the maximum voltage deflection to the corresponding current value. We took the median of all hyperpolarizing currents as the final input resistance value. In contrast, in the patch-clamp/morphology experiments, the current clamp before current stimulation was not always fixed at 0 pA. For that reason we used linear regression (for robustness, random sample consensus regression, as implemented in `scikit-learn`) of the steady state membrane voltage onto the current stimulation value to compute the input

679 resistance (regression slope) and the resting membrane potential (regression intercept) (Fig.
680 S1D). For this we used five highest hyperpolarizing currents (if there were fewer than five, we
681 used those available).
682
683 To estimate the rheobase (minimum current needed to elicit any spikes), we used robust
684 regression of the spiking frequency onto the stimulation current using the five lowest
685 depolarizing stimulation currents with non-zero spike count (if there fewer than five, we used
686 those available) (Fig. S1D). The point where the regression line crosses the *x*-axis gives the
687 rheobase estimate. We restricted the rheobase estimate to be between the highest current
688 clamp value eliciting no spikes and the lowest current clamp value eliciting at least one spike. In
689 the rare cases when the regression line crossed the *x*-axis outside of this interval, the nearest
690 edge of the interval was taken instead as the rheobase estimate.
691
692 The action potential (AP) threshold, AP amplitude, AP width, afterhyperpolarization (AHP),
693 afterdepolarization (ADP), and the first spike latency were computed as illustrated in Fig. S1C,
694 using the very first spike fired by the neuron. AP width was computed at the half AP height.
695 The adaptation index (AI) is defined as the ratio of the second interspike interval to the first one
696 (Fig. S1B). We took the median over the five lowest depolarizing current stimulation that elicited
697 at least three spikes (if fewer than five were available, we used all of them).
698
699 The maximum number of spikes simply refers to the maximum number of spikes emitted in the
700 600 ms stimulation window over all stimulation currents (Fig. S1A). The membrane time
701 constant (tau) was computed as the time constant of the exponential fit to the first phase of
702 hyperpolarization (median over all hyperpolarizing traces). Finally, the sag ratio is defined as the
703 ratio of the maximum membrane voltage deflection to the steady state membrane voltage during
704 the first (the lowest) hyperpolarizing current clamp stimulation.

705

706 **Data analysis of the electrophysiological features**

707 For the t-SNE visualization (Fig. 2B), we log-transformed the AI values because this feature had
708 a strongly right-skewed distribution (Fig. S1). We also excluded ADP and latency; ADP
709 because it was equal to zero for most neurons and rare cells with non-zero values appeared as
710 isolated subpopulations in the t-SNE representation, and latency because it had high outliers
711 among the FS types, also yielding isolated subpopulations. The remaining 11 features were *z*-
712 scored and exact (non-approximate) t-SNE was run with perplexity 15 and random initialisation
713 with seed 42 using `scikit-learn` implementation:

714 `TSNE(perplexity=15, method='exact', random_state=42)`

715 For pairwise classification, we used exactly the same procedure as described above for
716 pairwise classification using the reconstructed morphologies (nested cross-validation with
717 logistic regression regularized with elastic net). All 13 features were used, with log-transformed
718 AI and log-transformed latency (as shown in Fig. S1).

719

720 **Data analysis of the RNA-seq data**

721 Quality control

722 The total number of sequenced cells was *n*=118. Five cells were excluded because the sum of
723 counts across all genes (library size) was below 2000 (Fig. S3A). The remaining *n*=113 cells
724 were mapped to the full set of 133 transcriptomic clusters identified in Tasic et al. [18]; see below
725 for the details. Following this, one cell was excluded because it had correlation above 0.4 to one
726 of the non-neural clusters (Fig. S3B) and we considered it potentially contaminated with non-
727 neural RNA. One cell was excluded because it mapped to one of the excitatory clusters, and
728 three cells were excluded because they mapped to *Pvalb* clusters. All the remaining *n*=108 cells
729 mapped to the *Sst* clusters. Among those, five cells did not have good electrophysiological

recordings (the recordings were either lost or were of bad quality) and were excluded. This left *n*=103 cells for downstream analysis.

Mapping to the reference clusters

Using the count matrix of Tasic et al. (*n*=23,822, *d*=45,768), we selected 3000 "most variable" genes (see below). We then log-transformed all counts with $\log_2(x+1)$ transformation and averaged the log-transformed counts across all cells in each of the 133 clusters, to obtain reference transcriptomic profiles of each cluster (133×3000 matrix). Out of these 3000 genes, 2575 were present in the `mm10` reference genome that we used to align reads in our data (see above). We applied the same $\log_2(x+1)$ transformation to the read counts of our cells, and for each cell computed Pearson correlation across the 2575 genes with all 133 Tasic et al. clusters. Each cell was assigned to the cluster to which it had the highest correlation.

Gene selection

To select "most variable" genes, we found genes that had, at the same time, high non-zero expression and high probability of near-zero expression [69]. Our procedure is described in more detail elsewhere [48]. Specifically, we excluded all genes that had counts of at least 32 in fewer than 10 cells. For each remaining gene we computed the mean $\log_2$ count across all counts that were larger than 32 (non-zero expression, μ) and the fraction of counts that were smaller than 32 (probability of near-zero expression, τ). Across genes, there was a clear inverse relationship between μ and τ, that roughly followed exponential law $\tau \approx \exp(-\mu+a)$ for some horizontal offset *a*. Using a binary search, we found a value *b* of this offset that yielded 3000 genes with $\tau > \exp(-\mu+b) + 0.02$. These 3000 genes were selected.

Sometimes an exponential law with decay factor d=1.5 described the bulk of the gene population better. Then we used $\tau > \exp(-1.5\mu+b) + 0.02$ as the selection criterion. This is always explicitly mentioned below.

t-SNE

The t-SNE visualization of the whole Tasic et al. [18] dataset shown in Fig. S3C was taken from our previous work [48]. It was computed there using PCA initialization and perplexity combination of 50 and 500, following preprocessing steps of library size normalization (by converting counts to counts per million), feature selection (3000 most variable genes), $\log_2(x+1)$ transformation, and reducing the dimensionality to 50 using PCA.

To make t-SNE visualization of the somatostatin part of the Tasic et al. dataset (Fig. 4B), we selected all cells from all *Sst* clusters apart from the very distinct *Sst Chodl* (20 clusters, 2701 cells). Using these cells, we selected 500 most variable genes using the procedure described above with decay factor 1.5. We used the same preprocessing steps as above, perplexity 50, and initialised t-SNE with the respective coordinates from the full-dataset t-SNE, zero-centered and scaled to have the standard deviation of the first coordinate equal to 0.0001 [48]. This initialisation was only used for convenience as it makes the resulting t-SNE visualization "aligned" to the zoomed-in version of the full-dataset t-SNE.

Mapping to t-SNE

For each of the n=103 Patch-seq cells, we computed its Pearson correlation with each of the 2701 reference cells across the 500 genes, most variable in the somatostatin part of the Tasic et al. data set (only 472 genes present in our data were used). Then we found 10 reference cells with the maximal correlation (10 "nearest neighbours" of our cell) and positioned our cell at the median t-SNE location of those 10 reference cells [48].

780

781 Mapping to somatostatin clusters

782 The mapping of the *n*=103 Patch-seq cells to the 20 somatostatin clusters (Fig. 4C, S3) was
783 done exactly as the mapping to the full set of 133 clusters described above, but this time only
784 using 500 genes, most variable in the somatostatin part of the Tasic et al. [18] data set (only 472
785 genes present in our data were used).

786

787 Sparse reduced-rank regression

788 We used our implementation of sparse reduced-rank regression (RRR) described in detail
789 elsewhere [47]. For the analysis shown in Fig. 4E, we selected 500 most variable genes as
790 described above, using *n*=71 cells from L4 (the remaining cells among *n*=103 were from L5).
791 The gene counts were converted to counts per million and $\log_2(x+1)$-transformed. The columns
792 of the resulting 71×500 expression matrix were standardized. All electrophysiological features
793 were standardized as well. We used RRR with alpha=0.5, lambda=1, and rank 2 (with "relaxed
794 elastic net" [47]). Fig. 4E shows two standardized RRR components in the transcriptomic and in
795 the electrophysiological spaces. Features are depicted as lines showing correlations of a feature
796 with each of the two components. All features are shown in the electrophysiological space. Only
797 genes selected by the model are shown in the transcriptomic space. Additionally, all non-
798 selected genes that had root-sum-square correlation above 0.6 are shown with the dashed line.
799 Only one gene (*Hpse*) passed this threshold. This means that it was not selected by the model
800 (other genes, correlated with it, were selected instead), but it had high correlation to the
801 electrophysiological features. The value of R-squared and correlations between the components
802 from electrophysiological and transcriptomic spaces shown in Fig. 4E are cross-validation
803 estimates. We used hyperparameter values approximately maximizing cross-validated R-
804 squared.

805 For Fig. S5F, we used all *n*=103 cells. The procedure was identical.

806

Supplementary figures

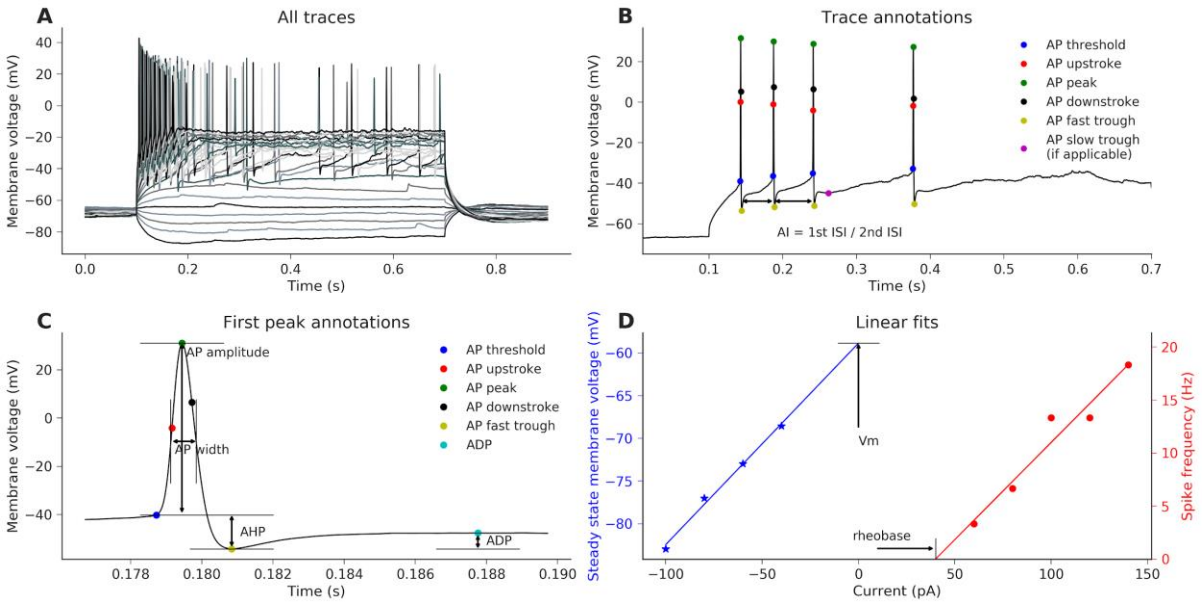

Figure S1: Schematic of the electrophysiological features and the extraction algorithm. All panels show data from the same exemplary Martinotti cell. (A) Responses to the consecutive current clamp stimulation currents. The maximum number of spikes elicited in 600 ms was 11. Hyperpolarizing currents are used to compute sag ratio (1.3) and membrane time constant tau (23.2 ms). (B) Zoom-in to one particular trace in (A) showing trace annotations and AI (1.13). (C) Zoom-in to the first spike elicited by this neuron. This action potential is used to compute AP threshold (-40.1 mV), AP amplitude (71.3 mV), AP width (0.72 ms), AHP (-14.1 mV), ADP (6.6 mV), and latency of the first spike (78.7 ms) (D) Blue regression line gives an estimate of resting membrane potential (-58.9 mV) and input resistance (235.8 MΩ). Red regression line gives a rheobase estimate (40 pA).

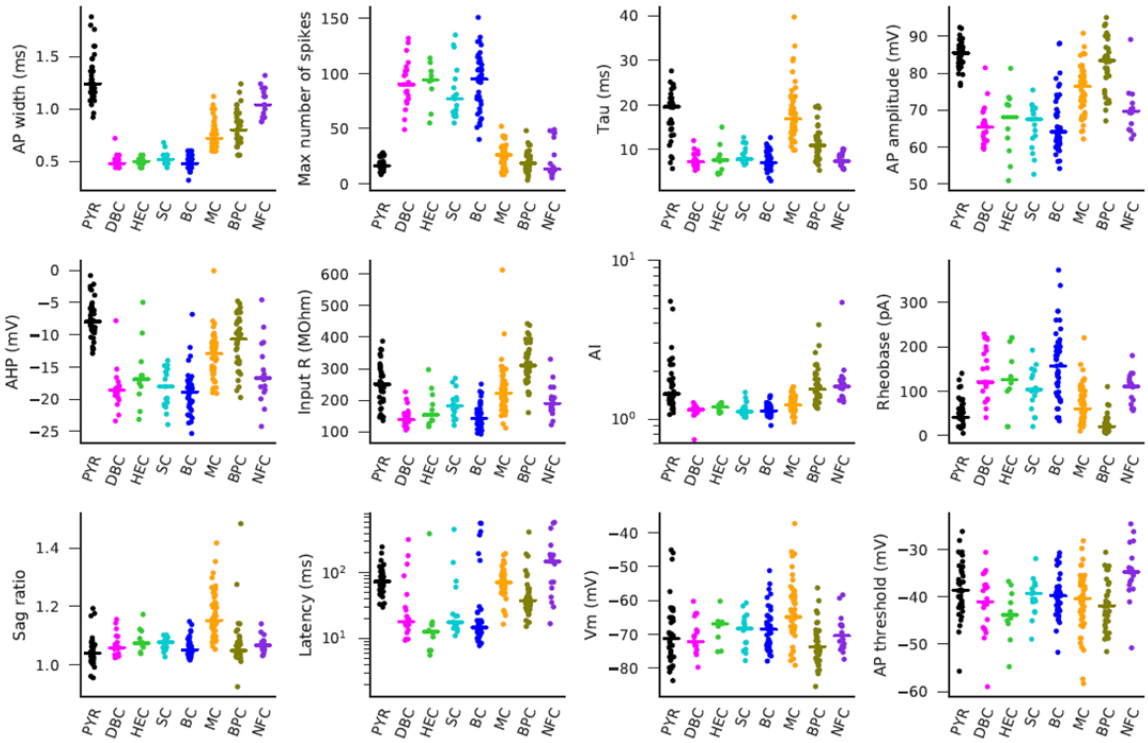

Figure S2: Electrophysiological features of neural cell types in V1 L4. Each panel shows one of the 13 automatically extracted electrophysiological features for *n*=235 neurons: action potential (AP) width, maximum number of spikes emitted during 600 ms of stimulation, membrane time constant tau, AP amplitude, afterhyperpolarization (AHP) depth, input resistance, adaptation index, rheobase, sag ratio, latency of the first spike, membrane potential, and AP threshold. Features are sorted by how strongly they varied between cell types (from the most strongly to the least strongly), as quantified by the Kruskal-Wallis test statistic. Horizontal lines show medians in each cell type. Afterdepolarization (ADP) height is not shown because its median was 0 for all cell types. See Fig. S1 for explanations of the feature.

Morphology of labeled neurons for mouse Cre line

Cell type / Cre-line	PYR	BC	MC	SC	BPC	NFC	DBC	HEC	NMC
Viiat V1 (n=47)	*11/245 (4.5%)*	*88/245 (35.5%)*	*47/245 (20.4%)*	*22/245 (8.9%)*	*29/245 (11.4%)*	*27/245 (11.0%)*	*13/245 (4.8%)*	*8/245 (3.2%)*	/
PV V1 (n=31)	/	*126/163 (77.3%)*	/	*15/163 (9.2%)*	/	/	*20/163 (12.2%)*	*2/163 (1.2%)*	/
VIP V1 (n=8)	/	/	/	/	*26/26 (100%)*	/	/	/	/
SCNN1A V1 p15/20 (n=5)	*17/17 (100%)*	/	/	/	/	/	/	/	/
SCNN1A V1 p30/40 (n=5)	*31/31 (100%)*	/	/	/	/	/	/	/	/
SCNN1A V1 >p 60 (n=5)	*30/30 (100%)*	/	/	/	/	/	/	/	/
SOM V1 (n=14)	/	5/61 (8.2%)	56/61 (91.8%)	/	/	/	/	/	/
SOM S1 (n=24)	/	1/79 (1.2%)	2/79 (2.5%)	/	/	/	/	/	76/79 (77.7%)

Figure S3. Morphological types of labeled neurons in different mouse Cre lines.

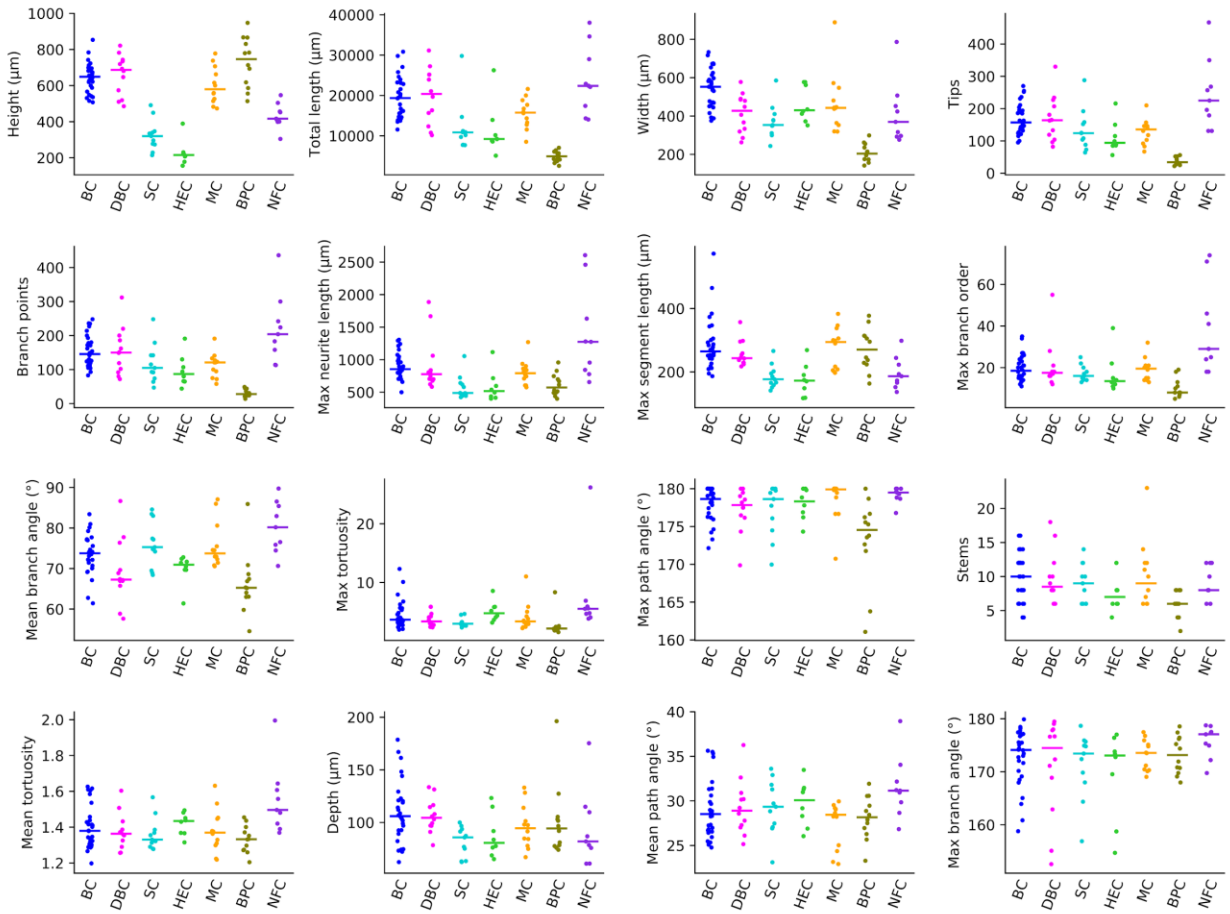

Figure S4: Morphological features of neural cell types in V1 L4. Each panel shows one of the 16 selected morphological summary statistics for *n*=92 neurons: height (extent along the cortical depth), total length of neurites, width (extent along the *x*-axis), number of tips, number of branch points, length of the longest neurite from tip to soma, length of the longest segment, maximum branch order, mean branch angle between two branches, maximum tortuosity, maximum path angle, number of stems extending from the soma, mean tortuosity, depth (extent along the *y*-axis), mean path angle and maximum branch angle. Features are sorted by how strongly they varied between cell types (from strongest to weakest), as quantified by the Kruskal-Wallis test statistic. Horizontal lines show medians in each cell type.

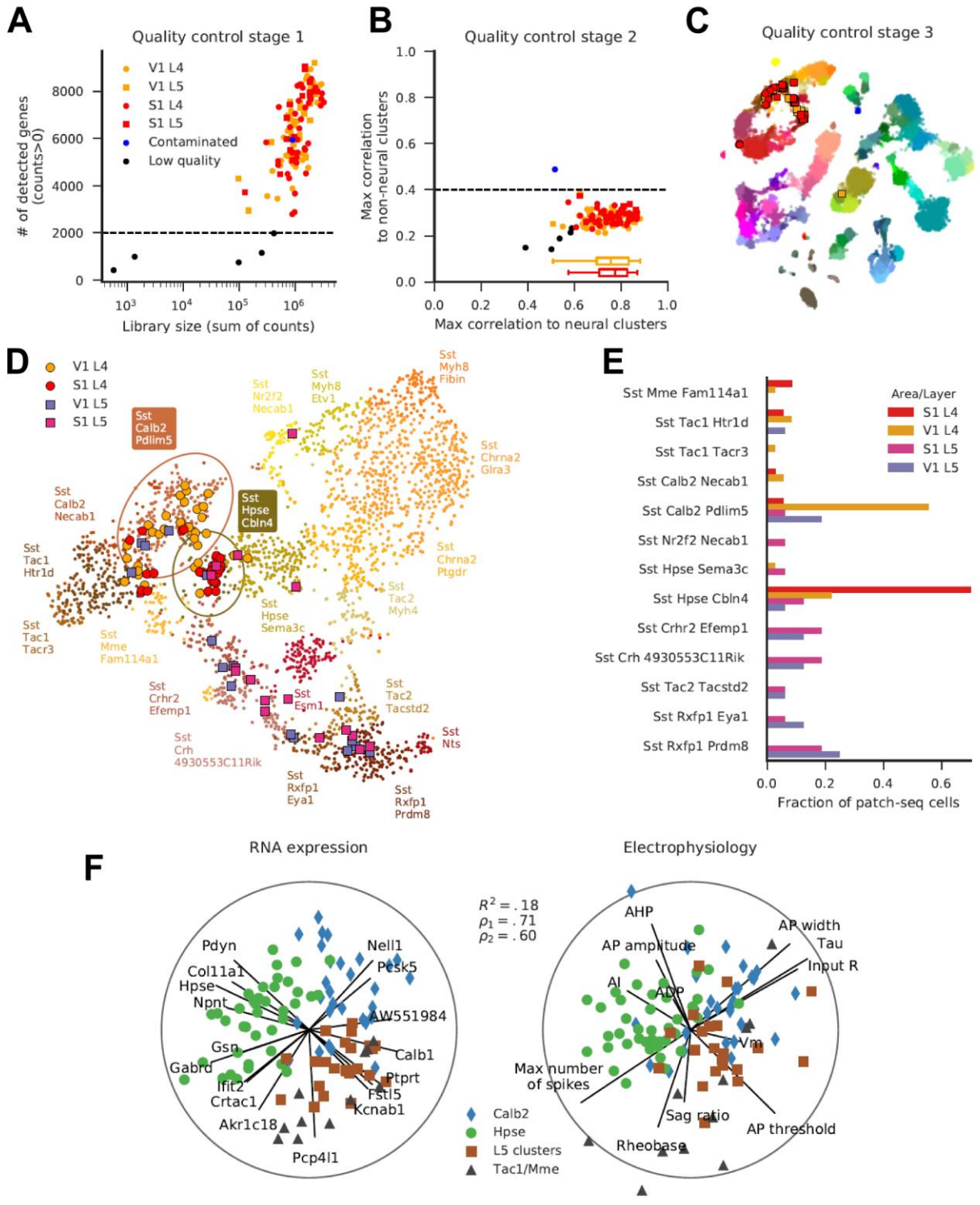

Figure S5: Quality control and data analysis for Patch-seq data including L5 cells. (A) Distribution of library sizes (total sum of gene counts) and numbers of detected genes (number of positive counts) for each sequenced cell (*n*=118). Five cells with less than 2000 genes detected were excluded. **(B)** For each

cell, we found its maximal correlation to the cluster means of the Tasic et al. [18] dataset across all neural clusters (*x*-axis) and across all non-neural clusters (*y*-axis). One cell that had a maximal correlation to non-neural clusters above 0.4 (presumably due to non-neural contamination) was excluded. Boxplots show distribution of maximal correlation for V1 and S1 cells. Correlations were not lower for S1 cells, despite the fact that the Tasic et al. dataset only contained data from V1 and ALM. **(C)** All *n*=112 remaining cells were positioned on the t-SNE map of the Tasic et al. dataset. Three cells that mapped to Pvalb clusters and one cell that mapped to excitatory clusters were excluded. Five of the remaining cells did not have a good electrophysiological recording. This left *n*=103 cells for further analysis. **(D)** Mapping of the Patch-seq cells (*n*=103) to the t-SNE visualization of the transcriptomic diversity among somatostatin clusters from Tasic et al. See Fig. 4B. **(E)** Cluster assignment of the Patch-seq cells. See Fig. 4C. **(F)** Sparse reduced-rank regression analysis. See Fig. 4E.

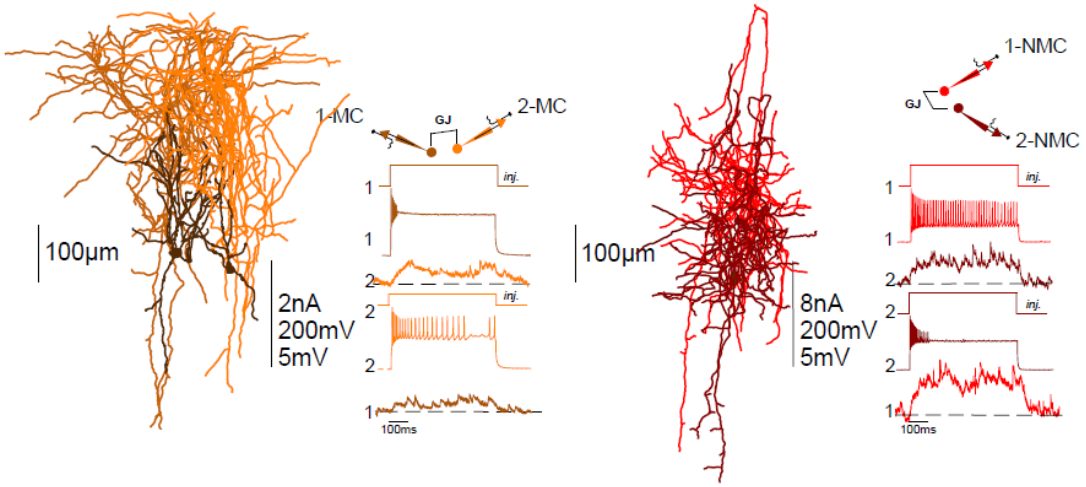

Figure S6: Gap junctions are common between both MCs and NMCs. Schematic representations of simultaneous recordings between L4 MCs in V1 (left) and L4 NMCs in S1 (right). Depolarizing current injections into either MC (left) or NMC (right) were transmitted to the other cell, confirming electrical coupling. The percentage of gap junctions was 23.5% in V1 (8/34) and 30.7% in S1 (8/26).

uI/EPSC (mV) in V1

POST \ PRE	PYR	BC	MC
PYR	0.75±0.13 mV PPR=75.6±5.1%	0.68±0.09 mV	0.50±0.07 mV
BC	1.17±0.13 mV PPR=85.8±6.5%	0.77±0.5 mV	0.59±0.09 mV
MC	/	0.53±0.15 mV	/

uI/EPSC (mV) in V1 among age

	PYR-PYR
p15/20	0.69±0.15 mV PPR=78.9±8.7%
p30/40	0.58±0.19 mV PPR=73.2±6.6%
>p 60	0.75±0.13 mV PPR=75.6±5.1%

uI/EPSC (mV) in S1

POST \ PRE	EXC	NMCs
EXC	0.99±0.12 mV PPR=87.2±4.0%	0.38±0.05 mV
NMC	0.53±0.16 mV PPR=139.±17.0%	0.19±0.05 mV

Figure S7. Amplitudes of uI(E)psc.

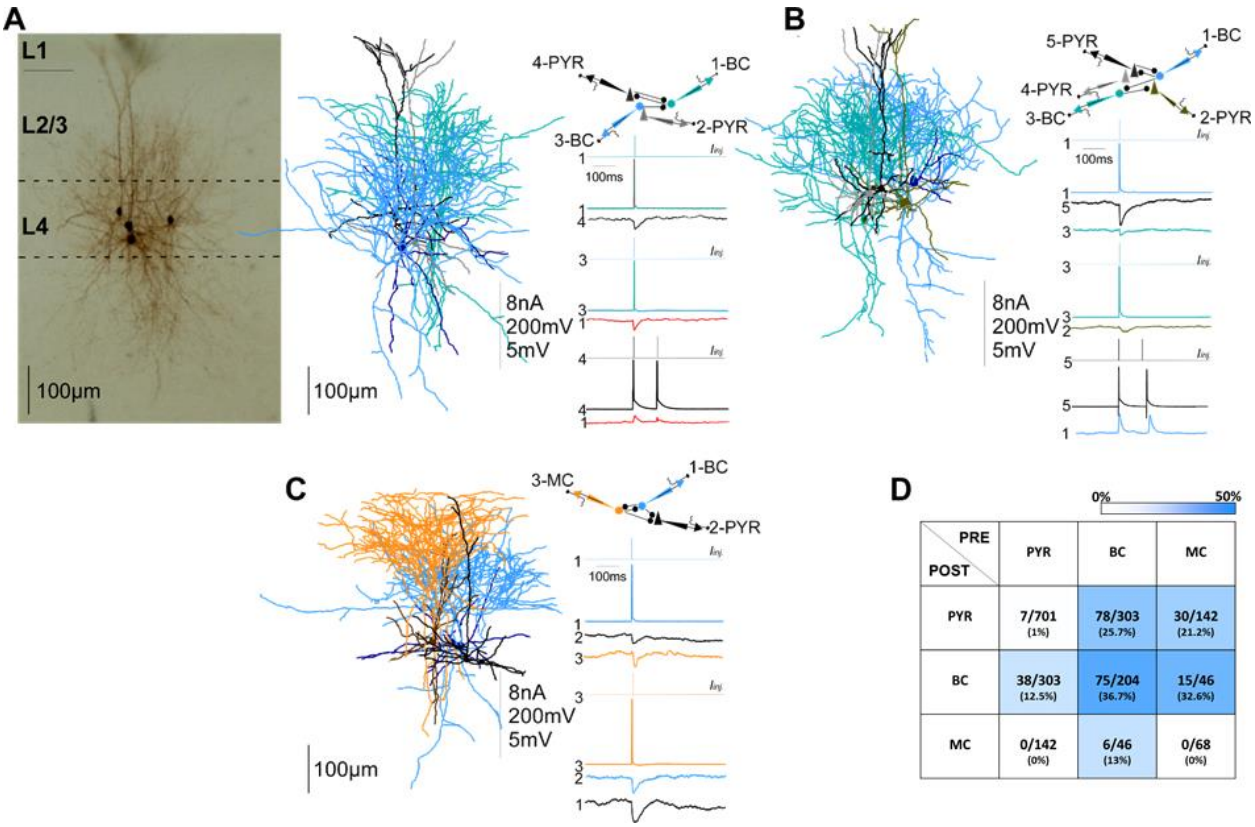

Figure S8: Connectivity between L4 PYRs, BCs, and MCs in V1. (A) On the left: Example of morphological recovery of four neurons. Recorded neurons were close to each other (generally less than 200µm). On the right: connection diagram of the same neurons, including two BCs and two PYRs, and their reconstructed morphology. Vertical scale bar indicates: amplitudes of injected current in nA, amplitude of APs in mV and amplitude of uEPSP or uIPSP in mV. **(B)** Connections between five simultaneously recorded neurons including three PYRs and two BCs. **(C)** Connections between three simultaneously recorded neurons including one PYR, one BC and one MC. **(D)** Color coded connectivity matrix showing the connection probabilities between PYRs, BCs and MCs computed as a fraction of all tested connections. Average of uEPSP and uIPSP as well as PPR are reported in Fig. S7.

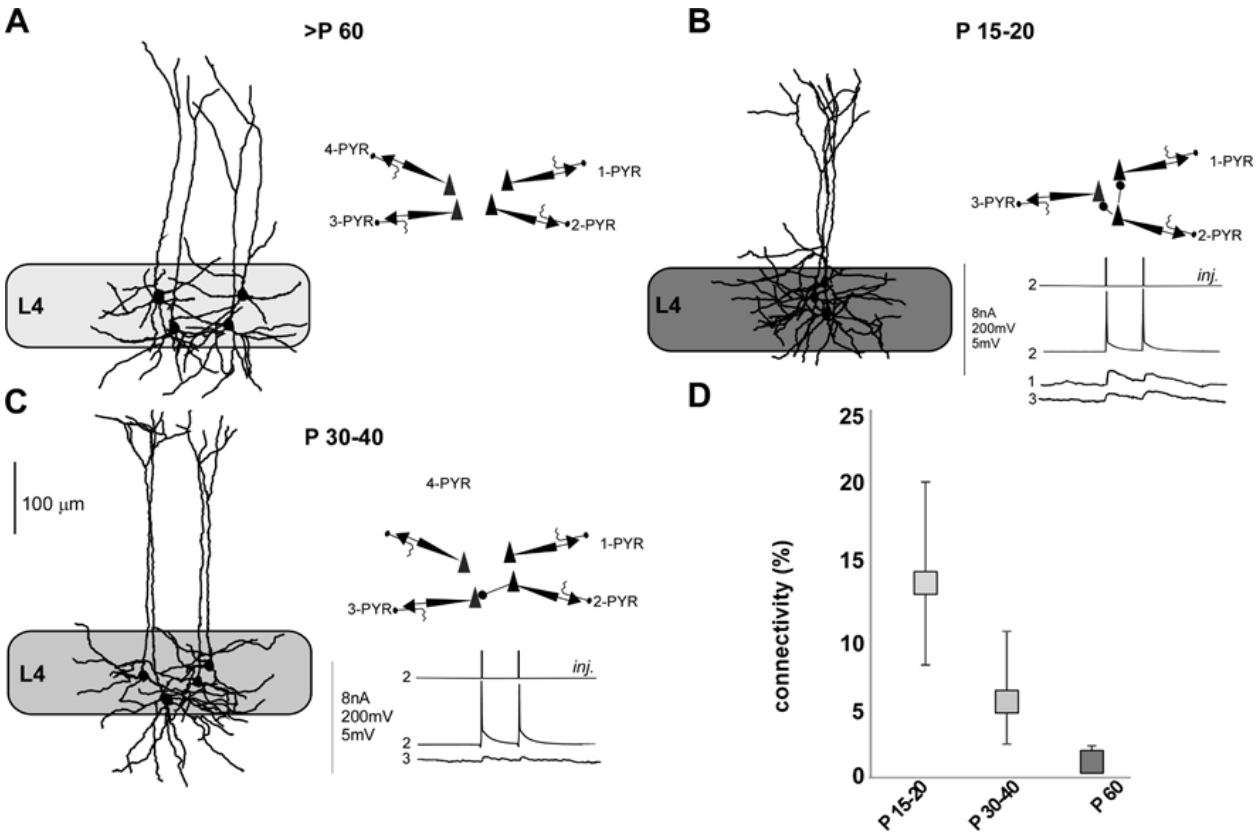

873

874

875 **Figure S9: Connectivity between PYRs in V1 L4 at different ages. (A-C)** Examples of simultaneously

876 recorded L4 neurons in >p60 (A), p15-20 (B), and p30-40 (C) mice. **(D)** Connectivity probability between

877 PYRs at different ages: 13.2% in p15-p20 (15/114), 5.1% in p30-p40 (8/156), and 1.0% in p60+ (7/701).

878 Error bars are 95% Clopper-Pearson confidence intervals.

879 ## Acknowledgements

880 Supported by the Intelligence Advanced Research Projects Activity (IARPA) via Department of
881 Interior/Interior Business Center (DoI/IBC) contract number D16PC00003. The U.S.
882 Government is authorized to reproduce and distribute reprints for Governmental purposes
883 notwithstanding any copyright annotation thereon. The views and conclusions contained herein
884 are those of the authors and should not be interpreted as necessarily representing the official
885 policies or endorsements, either expressed or implied, of IARPA, DoI/IBC, or the U.S.
886 Government.
887
888 This work was also supported by the German Research Foundation (BE5601/4-1, EXC 2064,
889 EXC 307, SFB1233), the Federal Ministry of Education and Research (FKZ 01GQ1601) and the
890 National Institute of Mental Health and the National Institute of Neurological Disorders And
891 Stroke under Award Number U19MH114830. The content is solely the responsibility of the
892 authors and does not necessarily represent the official views of the National Institutes of Health.
893

894 ## Author contributions

895 FS and XJ performed electrophysiological recordings and manual neuronal reconstructions. DK
896 directed the computational analysis. JC created full-length cDNA libraries and aided in
897 morphological recovery. LH prepared the full-length cDNA libraries for sequencing and
898 performed sequencing and initial bioinformatics analysis under the supervision of RS. ZT
899 sustained animals' colonies and provided experimental support. SL did the morphological data
900 analysis. YB did the electrophysiological data analysis. DK did the transcriptomic data analysis.
901 FS, DK, SL, YB analyzed the data and produced the figures. FS, KD, SS, and CCR wrote the
902 manuscript with input from PB. AT, XJ, and PB discussed and oversaw analysis and results. All
903 authors also revised the manuscript.

904

References

1. Staiger, J. F. Functional Diversity of Layer IV Spiny Neurons in Rat Somatosensory Cortex: Quantitative Morphology of Electrophysiologically Characterized and Biocytin Labeled Cells. *Cereb. Cortex* **14**, 690–701 (2004).
2. Petersen, C. C. H. & Sakmann, B. The Excitatory Neuronal Network of Rat Layer 4 Barrel Cortex. *J. Neurosci.* **20**, 7579–7586 (2000).
3. Callaway, E. M. & Borrell, V. Developmental sculpting of dendritic morphology of layer 4 neurons in visual cortex: influence of retinal input. *J. Neurosci.* **31**, 7456–7470 (2011).
4. Koelbl, C., Helmstaedter, M., Lübke, J. & Feldmeyer, D. A Barrel-Related Interneuron in Layer 4 of Rat Somatosensory Cortex with a High Intrabarrel Connectivity. *Cereb. Cortex* **25**, 713–725 (2013).
5. Emmenegger, V., Qi, G., Wang, H. & Feldmeyer, D. Morphological and Functional Characterization of Non-fast-Spiking GABAergic Interneurons in Layer 4 Microcircuitry of Rat Barrel Cortex. *Cereb. Cortex* **28**, 1439–1457 (2018).
6. Yavorska, I. & Wehr, M. Somatostatin-Expressing Inhibitory Interneurons in Cortical Circuits. *Front. Neural Circuits* **10**, (2016).
7. Ma, Y. Distinct Subtypes of Somatostatin-Containing Neocortical Interneurons Revealed in Transgenic Mice. *Journal of Neuroscience* **26**, 5069–5082 (2006).
8. Xu, H., Jeong, H.-Y., Tremblay, R. & Rudy, B. Neocortical somatostatin-expressing GABAergic interneurons disinhibit the thalamorecipient layer 4. *Neuron* **77**, 155–167 (2013).
9. Cruikshank, S. J., Lewis, T. J. & Connors, B. W. Synaptic basis for intense thalamocortical activation of feedforward inhibitory cells in neocortex. *Nat. Neurosci.* **10**, 462–468 (2007).
10. Beierlein, M., Gibson, J. R. & Connors, B. W. Two Dynamically Distinct Inhibitory Networks in Layer 4 of the Neocortex. *J. Neurophysiol.* **90**, 2987–3000 (2003).

11. Higley, M. J. & Contreras, D. Balanced excitation and inhibition determine spike timing during frequency adaptation. *J. Neurosci.* **26**, 448–457 (2006).
12. Gabernet, L., Jadhav, S. P., Feldman, D. E., Carandini, M. & Scanziani, M. Somatosensory Integration Controlled by Dynamic Thalamocortical Feed-Forward Inhibition. *Neuron* **48**, 315–327 (2005).
13. Kloc, M. & Maffei, A. Target-specific properties of thalamocortical synapses onto layer 4 of mouse primary visual cortex. *J. Neurosci.* **34**, 15455–15465 (2014).
14. Cruikshank, S. J., Urabe, H., Nurmikko, A. V. & Connors, B. W. Pathway-specific feedforward circuits between thalamus and neocortex revealed by selective optical stimulation of axons. *Neuron* **65**, 230–245 (2010).
15. Kawaguchi, Y. & Kubota, Y. GABAergic cell subtypes and their synaptic connections in rat frontal cortex. *Cereb. Cortex* **7**, 476–486 (1997).
16. Ikan, R. *Naturally Occurring Glycosides*. (Wiley, 1999).
17. Ma, Y., Hu, H. & Agmon, A. Short-term plasticity of unitary inhibitory-to-inhibitory synapses depends on the presynaptic interneuron subtype. *J. Neurosci.* **32**, 983–988 (2012).
18. Tasic, B. *et al.* Shared and distinct transcriptomic cell types across neocortical areas. *Nature* **563**, 72–78 (2018).
19. Nowakowski, T. J. *et al.* Regulation of cell-type-specific transcriptomes by microRNA networks during human brain development. *Nat. Neurosci.* **21**, 1784–1792 (2018).
20. Xu, X. *et al.* Primary visual cortex shows laminar-specific and balanced circuit organization of excitatory and inhibitory synaptic connectivity. *J. Physiol.* **594**, 1891–1910 (2016).
21. Jiang, X. *et al.* Principles of connectivity among morphologically defined cell types in adult neocortex. *Science* **350**, aac9462–aac9462 (2015).
22. Cadwell, C. R. *et al.* Multimodal profiling of single-cell morphology, electrophysiology, and gene expression using Patch-seq. *Nat. Protoc.* **12**, 2531–2553 (2017).
23. Cadwell, C. R. *et al.* Electrophysiological, transcriptomic and morphologic profiling of single

neurons using Patch-seq. *Nat. Biotechnol.* **34**, 199–203 (2016).

24. Fuzik, J. *et al.* Integration of electrophysiological recordings with single-cell RNA-seq data identifies neuronal subtypes. *Nat. Biotechnol.* **34**, 175–183 (2016).
25. Ramaswamy, S. & Markram, H. Anatomy and physiology of the thick-tufted layer 5 pyramidal neuron. *Front. Cell. Neurosci.* **9**, 233 (2015).
26. Romand, S., Wang, Y., Toledo-Rodriguez, M. & Markram, H. Morphological Development of Thick-Tufted Layer V Pyramidal Cells in the Rat Somatosensory Cortex. *Front. Neuroanat.* **5**, (2011).
27. Kim, E. J., Juavinett, A. L., Kyubwa, E. M., Jacobs, M. W. & Callaway, E. M. Three Types of Cortical Layer 5 Neurons That Differ in Brain-wide Connectivity and Function. *Neuron* **88**, 1253–1267 (2015).
28. Xue, M., Atallah, B. V. & Scanziani, M. Equalizing excitation–inhibition ratios across visual cortical neurons. *Nature* **511**, 596–600 (2014).
29. Harris, J. A. *et al.* Anatomical characterization of Cre driver mice for neural circuit mapping and manipulation. *Front. Neural Circuits* **8**, 76 (2014).
30. Chao, H. T. *et al.* Dysfunction in GABA signalling mediates autism-like stereotypies and Rett syndrome phenotypes. *Nature* **468**, 263–269 (2010).
31. Markram, H. *et al.* Interneurons of the neocortical inhibitory system. *Nat. Rev. Neurosci.* **5**, 793–807 (2004).
32. Petilla Interneuron Nomenclature Group *et al.* Petilla terminology: nomenclature of features of GABAergic interneurons of the cerebral cortex. *Nat. Rev. Neurosci.* **9**, 557–568 (2008).
33. DeFelipe, J. *et al.* New insights into the classification and nomenclature of cortical GABAergic interneurons. *Nat. Rev. Neurosci.* **14**, 202–216 (2013).
34. Wang, Y. *et al.* Anatomical, physiological and molecular properties of Martinotti cells in the somatosensory cortex of the juvenile rat. *J. Physiol.* **561**, 65–90 (2004).
35. Le Bon-Jego, M. & Yuste, R. Persistently active, pacemaker-like neurons in neocortex.

Front. Neurosci. **1**, 123–129 (2007).

36. Buchanan, K. A. *et al.* Target-Specific Expression of Presynaptic NMDA Receptors in Neocortical Microcircuits. *Neuron* **75**, 451–466 (2012).
37. Wang, Y., Gupta, A., Toledo-Rodriguez, M., Wu, C. Z. & Markram, H. Anatomical, physiological, molecular and circuit properties of nest basket cells in the developing somatosensory cortex. *Cereb. Cortex* **12**, 395–410 (2002).
38. Muñoz, W., Tremblay, R. & Rudy, B. Channelrhodopsin-Assisted Patching: InVivo Recording of Genetically and Morphologically Identified Neurons throughout the Brain. *Cell Rep.* **9**, 2304–2316 (2014).
39. Lund, J. S., Henry, G. H., MacQueen, C. L. & Harvey, A. R. Anatomical organization of the primary visual cortex (area 17) of the cat. A comparison with area 17 of the macaque monkey. *J. Comp. Neurol.* **184**, 599–618 (1979).
40. Saint Marie, R. L. & Peters, A. The morphology and synaptic connections of spiny stellate neurons in monkey visual cortex (area 17): a Golgi-electron microscopic study. *J. Comp. Neurol.* **233**, 213–235 (1985).
41. Anderson, J. C., Douglas, R. J., Martin, K. A. & Nelson, J. C. Map of the synapses formed with the dendrites of spiny stellate neurons of cat visual cortex. *J. Comp. Neurol.* **341**, 25–38 (1994).
42. Stratford, K. J., Tarczy-Hornoch, K., Martin, K. A. C., Bannister, N. J. & Jack, J. J. B. Excitatory synaptic inputs to spiny stellate cells in cat visual cortex. *Nature* **382**, 258–261 (1996).
43. Feldmeyer, D., Roth, A. & Sakmann, B. Monosynaptic connections between pairs of spiny stellate cells in layer 4 and pyramidal cells in layer 5A indicate that lemniscal and paralemniscal afferent pathways converge in the infragranular somatosensory cortex. *J. Neurosci.* **25**, 3423–3431 (2005).
44. Tasic, B. & Nicovich, P. R. Cell types behaving in their natural habitat. *Science* **362**, 749–

750 (2018).

45. Paul A, E. al. Transcriptional Architecture of Synaptic Communication Delineates GABAergic Neuron Identity. - PubMed - NCBI. Available at: https://www.ncbi.nlm.nih.gov/pubmed/28942923. (Accessed: 20th December 2018)
46. Naka, A. *et al.* Complementary networks of cortical somatostatin interneurons enforce layer specific control. (2018). doi:10.1101/456574
47. Kobak, D., Weis, M. A. & Berens, P. Sparse reduced-rank regression for exploratory visualization of single cell patch-seq recordings. (2018). doi:10.1101/302208
48. Kobak, D. & Berens, P. The art of using t-SNE for single-cell transcriptomics. (2018). doi:10.1101/453449
49. Pfeffer, C. K., Xue, M., He, M., Huang, Z. J. & Scanziani, M. Inhibition of inhibition in visual cortex: the logic of connections between molecularly distinct interneurons. *Nat. Neurosci.* **16**, 1068–1076 (2013).
50. Galarreta, M. & Hestrin, S. Electrical synapses between GABA-releasing interneurons. *Nat. Rev. Neurosci.* **2**, 425–433 (2001).
51. Markram, H., Lübke, J., Frotscher, M., Roth, A. & Sakmann, B. Physiology and anatomy of synaptic connections between thick tufted pyramidal neurones in the developing rat neocortex. *J. Physiol.* **500**, 409–440 (1997).
52. Song, S., Sjöström, P. J., Reigl, M., Nelson, S. & Chklovskii, D. B. Correction: Highly Nonrandom Features of Synaptic Connectivity in Local Cortical Circuits. *PLoS Biol.* **3**, e350 (2005).
53. Gibson, J. R., Beierlein, M. & Connors, B. W. Two networks of electrically coupled inhibitory neurons in neocortex. *Nature* **402**, 75–79 (1999).
54. Gouwens, N. W. *et al.* Classification of electrophysiological and morphological types in mouse visual cortex. *bioRxiv* 368456 (2018). doi:10.1101/368456
55. Larkum, M. A cellular mechanism for cortical associations: An organizing principle for the

cerebral cortex. *Trends Neurosci.* **36**, 141–151 (2013).

56. Lovett-Barron, M. *et al.* Regulation of neuronal input transformations by tunable dendritic inhibition. *Nat. Neurosci.* **15**, 423–30, S1–3 (2012).
57. Lodato, S. *et al.* Excitatory Projection Neuron Subtypes Control the Distribution of Local Inhibitory Interneurons in the Cerebral Cortex. *Neuron* **69**, 763–779 (2011).
58. Wong, F. K. *et al.* Pyramidal cell regulation of interneuron survival sculpts cortical networks. *Nature* **557**, 668–673 (2018).
59. Kapfer, C., Glickfeld, L. L., Atallah, B. V. & Scanziani, M. Supralinear increase of recurrent inhibition during sparse activity in the somatosensory cortex. *Nat. Neurosci.* **10**, 743–753 (2007).
60. Silberberg, G. & Markram, H. Disynaptic inhibition between neocortical pyramidal cells mediated by Martinotti cells. *Neuron* **53**, 735–746 (2007).
61. Adesnik, H., Bruns, W., Taniguchi, H., Huang, Z. J. & Scanziani, M. A neural circuit for spatial summation in visual cortex. *Nature* **490**, 226–231 (2012).
62. Jiang, X. *et al.* Response to Comment on 'Principles of connectivity among morphologically defined cell types in adult neocortex'. *Science* **353**, 1108 (2016).
63. Barth, A. *et al.* Comment on 'Principles of connectivity among morphologically defined cell types in adult neocortex'. *Science* **353**, 1108 (2016).
64. Qi, G., Radnikow, G. & Feldmeyer, D. Electrophysiological and Morphological Characterization of Neuronal Microcircuits in Acute Brain Slices Using Paired Patch-Clamp Recordings. *J. Vis. Exp.* 21–27 (2015).
65. Ramsköld, D., Wang, E. T., Burge, C. B. & Sandberg, R. An abundance of ubiquitously expressed genes revealed by tissue transcriptome sequence data. *PLoS Comput. Biol.* **5**, e1000598 (2009).
66. Jefferis, G. S. X. E. *et al.* Comprehensive maps of Drosophila higher olfactory centers: spatially segregated fruit and pheromone representation. *Cell* **128**, 1187–1203 (2007).

67. Li, Y., Wang, D., Ascoli, G. A., Mitra, P. & Wang, Y. Metrics for comparing neuronal tree shapes based on persistent homology. *PLoS One* **12**, e0182184 (2017).

68. Friedman, J., Hastie, T. & Tibshirani, R. Regularization Paths for Generalized Linear Models via Coordinate Descent. *J. Stat. Softw.* **33**, (2010).

69. Andrews, T. S. & Hemberg, M. Dropout-based feature selection for scRNASeq. *bioRxiv* 065094 (2018). doi:10.1101/065094